UNIVERSITÀ DEGLI STUDI DI NAPOLI FEDERICO II

C.I.R.A.M. – Interdepartmental Centre for Environmental Research

PhD School in Earth Sciences

PhD Course in
Environmental System Analysis

XXVIII cycle

PhD thesis

MHODE inversion of potential fields

Mahak Singh Chauhan

Tutor:
Prof. Maurizio Fedi

Co-tutor:
Prof. Mrinal K. Sen

PhD Coordinator:
Prof. Maurizio Fedi

2017

A mio padre e mia madre

To my parents

Contents

List of Figures

List of Tables

Summary

In this thesis, I describe a nonlinear method to invert potential fields data, based on inverting the scaling function (τ) of the potential fields - a quantity that is independent on the source property, that is mass density in gravity case or the magnetic susceptibility in the magnetic case. In this approach no a priori prescription of the density contrast is needed and the source model geometry is determined independently of it. We assume Talwani's formula and generalize the Multi-HOmogeneity Depth Estimation (MHODE) method to the case of the inhomogeneous field generated by a general 2D source. The scaling function is calculated at different altitudes along the lines defined by the extreme points of the potential fields and the inversion of the scaling function yields the coordinates of the vertices of a multiple source body with complex geometrical shape. Once the geometry is estimated, the source density is automatically computed from a simple regression of the scaling function of the gravity data vs. that generated from the estimated source body with unit density.

We solve the above nonlinear problem by the Very Fast Simulated Annealing algorithm. The best performance is obtained when some vertices are constrained by either reasonable bounds or exact knowledge. In the salt-dome case we assumed that the top of the body is known from seismic and we solved for the lateral and bottom parts of the body. We applied the technique on data from three synthetic cases of complex sources and on the gravity anomalies over the Mors salt-dome (Denmark) and the Godavari Basin (India). In all these cases, the method performed very well in terms of both geometrical and source-property definition.

1 Introduction

Geophysics is a science involving physics, mathematics and geology, addressed to the understanding of the complexity and heterogeneity of the Earth. Such heterogeneities occur because of the very diverse internal composition of the Earth that can be characterized by variations in their physical properties.

Geophysical studies, in practice, measure the change in physical quantities with respect to time and distance. Each geophysical method is associated with one or more physical property of the Earth, such as mass contrast in gravity or resistivity variation in electrical methods.

Evaluating the potential of oil or gas deposits, or energy and environmental resources in general (i.e. minerals and water), requires the integration of information collected from geology, drilling, seismology, electromagnetics, potential fields and others. The goal, is, obviously, gaining a good volumetric estimate of the physical property and planning to discover the resources production in the finest way.

Potential field methods, mainly gravity and magnetic methods, are among the oldest methods used in exploring the Earth interior. Despite the increasing role of other geophysical methods, some of which having better subsurface resolution, the gravity and magnetic methods continue to have an important role, thanks to their passive nature and to their successful contribution in deep and challenging environments, such as sub-salt structures and deep sea, to their smaller cost and to new powerful methods of analysis and modelling, which are indeed related to new high-quality and high-resolution data.

Moreover, information provided by inverting gravity and magnetic data can help to refine the targets and minimize the risk of investigation before the actual potential is defined. Additionally, these methods can be successfully applied in the environmental and engineering areas of interest, to assess the size of existing issues, to mitigate consequences and lead future drilling tests. Once measured data have been analyzed and interpreted, the results can also be used as input to model various systems, to prevent future environmental and engineering critical situations.

Inversion and imaging methods are the most valuable methods to retrieve automatically or semi-automatically the relevant information from the potential field data. The main focus of this thesis is on the development of a new inversion technique for interpreting inhomogeneous potential field data generated by complex sources.

1.1 Background of inverse problem:

Potential field data inversion is a very active research field, and each year new methods or variants to existing methods are proposed. The major advantages of inverse methods include automatic generation of the source parameters and the flexibility to account for different forms of a priori information about the unknown source distribution.

We must first distinguish between linear and non-linear inverse problems. In a linear problem, forward modeling involves application of a linear operator to the data. The solution of such problem typically involves the search for a solution minimizing a function, called the objective function.

However, the ill-posed nature of the problem requires some a priori information. The objective function usually assumes the following form:

$$\varphi = \varphi_d + \mu \varphi_m \quad ,$$

where the first term, φ_d, is usually expressed as $\|\mathbf{W}_d(\mathbf{Am}-\mathbf{d})\|^2$, that is the weighted misfit functional, where $\mathbf{d}$ are the observed data, $\mathbf{A}$ is the matrix kernel, $\mathbf{m}$ is the unknown model and $\mathbf{W}_d$ is the inverse data covariance or a data weighting matrix. μ is the regularization parameter, assessing the balance between the opposite requirements of fitting the data and satisfying the a priori information, expressed in the second term, called model objective function. φ_m is usually expressed as $\|\mathbf{W}_m(\mathbf{m}-\mathbf{m}_0)\|^2$, that is the weighted minimum-norm solution with respect to a reference model $\mathbf{m}_0$. Several types of constraints may be included in φ_m, such as density/magnetization spatial gradients, model depth-weighting, compactness/smoothing stabilizers, directional operators, sparseness constraints and bounds/constraints for the model, the closeness to some "a priori" model and so on (e.g., Li and Oldenburg, 1996; 1998; Pilkington, 1997; Zhdanov, 2002; Cella and Fedi, 2012). As regards the constraints, Paoletti et al., (2014) presented a self-

constrained inversion procedure based not only on external constraints (geophysical/geological information, drill logs), but also on self-constraints, such as depth, structural index, horizontal position and dip of the source edges, that are estimated in advance by apposite methods of analysis of potential field anomalies.

Adding specific requirements to the solution, such as a priori information on density bounds, may transform the linear problem into a nonlinear problem and specific algorithms are required, such as the conjugate gradients, to get the solution through an iterative cycle; preconditioning may speed up the process (Zhdanov, 2002; Pilkington, 1997).

Non-linear problems are usually solved by local optimization methods, that involve local linearization, but the solution is largely affected by the choice of a starting model. In fact, for nonlinear problems, many minima of different importance are likely to occur; this means that gradient-based local optimization algorithms are only suitable if **m** is close to some "a priori" model $\mathbf{m}_0$. A completely different class of inverse methods for nonlinear problems involves a search based on randomly sampling the model-space, with a directivity to guide the search. These methods include global optimization methods, such as simulated annealing (SA) and genetic algorithms (GAs) (Dimri, 1992; Sen and Stoffa, 2013). Applications of such methods, or combinations of global and local methods, have been exploited for potential field inversion by some authors (e.g., Zidarov and Zhelev, 1970; René, 1986; Camacho et al., 2000; Nagihara and Hall, 2001; Krahenbuhl and Li, 2006; Uieda and Barbosa, 2012). All of these methods, however assume prefixed values for the density contrast.

1.2 Ambiguity of the inverse problem:

It is well known that the interpretation of potential field data is characterized by inherent ambiguity (e.g., Roy, 1962). This means that many different models can generate exactly the same anomaly, as shown by Skeels (1947, Figure 1). Even considering a subset of the gravity sources, i.e. those being homogeneous in density, it is impossible to invert uniquely the data for their volume and density.

A different approach is inverting for the depth and shape of the source without needing the density to be known. This approach is inherent in Euler Deconvolution

(Thompson, 1982; Reid et al., 1990) and in some other methods, such as the interface determination under a priori information about two upper and lower depth limits (Fedi and Rapolla, 1999).

In this thesis, we adopt this last kind of approach and will invert the problem based on a function which does not depend on the density, namely the scaling function (Fedi, 2007). In order to solve this inverse problem we will use limited prior information about general depth bounds and depth at some points. The new inverse method consists of solving a set of nonlinear equations of the scaling function (Fedi, 2007) for the unknown vertex positions of a source model, defined according to the Talwani's formula (1959).

The scaling function defines the behaviour of potential fields vs. scales, or altitudes, independent of the source property (Fedi, 2007). It may be easily computed from the gravity measurements and, as shown in Fedi (2007), it assumes a very simple analytical expression when homogeneous fields are concerned. Since Talwani's formula allows us to consider source models generating inhomogeneous fields, we will use, in particular, the Multi Homogeneous Depth Estimation MHODE method (Fedi et al., 2015), which is based on the interpretation of the scaling function for a general field, either homogeneous or inhomogeneous. A very fast simulated-annealing algorithm (VFSA, Ingber, 1989; Sen and Stoffa, 1995) is used here to solve efficiently our nonlinear problem.

MHODE method performs very well for complex sources and allows the general ambiguity to be reduced. For instance, consider the simple case of a dipping dike.

Let us assume to know the top of the source from external information and try to deduce the bottom from inverting the gravity field. We first performed the gravity data inversion using the VFSA algorithm. As expected, the inversion based on the gravity data produced many models, all relatively close to the true one, characterized by different density contrasts (Figure 1.1) and it is difficult to choose the correct model without any external geological information about the source since the data produced by these models fit equally well the observed gravity data (Chauhan and Fedi, 2015). We then inverted the scaling function (Figure 1.2) and were able to retrieve successfully the bottom part of the body without any priori information about the density.

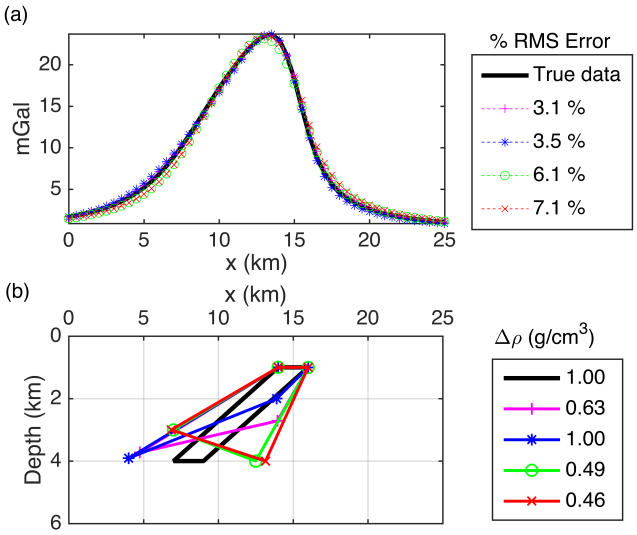

Figure 1.1 Inversion of a single-scale gravity anomaly, at z=0 km. Top: The gravity anomaly (black) and the computed anomalies from the inverted source models; Bottom: True source (black line) and inverted source models. Different colours indicate different densities.

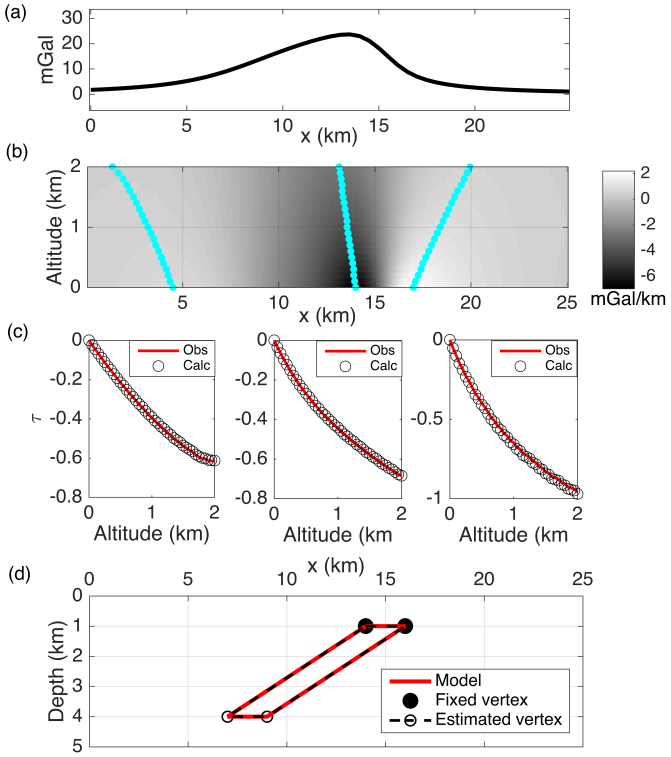

Figure 1.2 Inversion of the scaling function on a multiscale dataset. a) gravity anomaly; b) Multiscale 1st order derivative gravity field with ridges (cyan curves); c) scaling function for each cyan ridge; d) Source model. The top of the source is fixed (black solid dots), leaving the bottom vertices to be estimated by inversion (black circles).

In the following chapters of this thesis, we will discuss the main theoretical aspects that are used in this research project, starting from a brief description of some potential field methods and functional transformations. We will then describe the MHODE method in detail and the modifications we introduced in the related inverse problem by using the VFSA method. Then we will discuss the application of these algorithms to several synthetic cases corresponding to a 2D salt-dome model, assuming realistic scenarios, and then to two real cases: the gravity data of the Mors salt dome (Denmark) and of the Gadavari basin (India).

2 Potential fields Theory

At any point of the space, a unit mass, a unit charge or a magnetic dipole experience certain kind of forces. These forces can be repulsive, like between two poles of the same polarity for the electric field or attractive as for the gravitational field (Roy, 2008). In general, these forces are called field of forces. These fields follow laws that were defined in mathematical form by many scientists throughout the time. In geophysics, we enjoy the physical nature of these fields to image the subsurface.

Force fields act in the space at a given time (Blakely, 1996). Examples of force fields are the gravitational field and the magnetic field of the Earth. Fields can be classified in two categories, either vector or scalar. For examples, rock density or gas temperature at a certain point and time are scalar fields. Gravitational attraction, heat flow and velocity of the fluid are examples of vector fields (Blakely, 1996).

Mathematically, if the field **F**, having a scalar potential ϕ given by $F = \nabla\phi$ (or $F = -\nabla\phi$), is conservative then the field **F** is named potential field and satisfies the *Laplace's equation* in the region out of the sources:

$$\nabla^2\phi = 0. \tag{2.1}$$

This means that the sum of the rates of change of the field gradient in three orthogonal directions is zero (Kearey et al., 2002). In Cartesian coordinates *Laplace's equation* is:

$$\frac{\partial^2\phi}{\partial x^2} + \frac{\partial^2\phi}{\partial y^2} + \frac{\partial^2\phi}{\partial z^2} = 0, \tag{2.2}$$

where ϕ refer to the gravitational and magnetic potentials.

Following the above remarks, we may define harmonic functions. Following Blakely (1996), any function that satisfy the *Laplace's equation*, has continuous, single-

valued derivatives and has second derivatives. If a function is harmonic in a region R, do not have the maxima and minima within the region except on boundaries but the converse may not be true.

Gravity and magnetic fields, are both potential field methods and obey all the physical criteria mentioned above. A brief description about these methods is given in the following section.

2.1 Gravity Method

The gravitation field is defined in terms of gravitational potential or Newtonian Potential U:

$$U = \frac{\gamma M}{r}, \tag{2.3}$$

where γ is the gravitational constant, M is the mass of the Earth and r is the distance from the center of the Earth.

The gravitational potential is a scalar quantity, whereas gravitational acceleration is a vector quantity having the direction vertically downward. First-order directional derivatives of U are the components of gravity in the corresponding direction (Kearey et al., 2002) and it is defined as:

$$\mathbf{g} = \nabla U = \frac{\partial U}{\partial x}\mathbf{i} + \frac{\partial U}{\partial y}\mathbf{j} + \frac{\partial U}{\partial z}\mathbf{k}, \tag{2.4}$$

where $\mathbf{i}, \mathbf{j}$ and $\mathbf{k}$ are the unit vectors in the positive direction of x, y and z axes respectively. Equation 2.4 can be extended to calculate the gradient of any gravity field components.

The gravitational potential is harmonic at all the points outside of the mass that yields $\nabla^2 U = 0$, but in the space occupied by masses:

$$\nabla^2 U = -4\pi\gamma\rho, \tag{2.5}$$

where ρ is the density of the mass distribution at a given point.

This is the *Poisson's equation* that describe the potential at all points of the mass distribution.

In geophysical exploration, gravimeters measure only the vertical component of the gravity, as given by:

$$g_z = \frac{\partial g}{\partial z}. \qquad 2.6$$

For any objective of applying gravity method, the collected data during surveying need the corrections for all the variation in the Earth's gravitational field which do not result from the difference of density of the underlying rocks. The observed gravity is the sum of the following components (Blakely, 1996):

- attraction of the reference ellipsoid (theoretical gravity).
- effect of elevation above sea level (free air effect).
- effect of "normal" mass above sea level (Bouguer slab and terrain effects).
- time-dependent variations (tidal and instrumental drift effects).
- effect of moving platform (Eötvös effect).
- effect of masses that support topographic loads (isostatic effects).
- effect of crust and upper mantle density variations ("geology").

The main aim is to isolate the last quantity – the effect of the density variations in crustal and upper mantle from all other terms. This process is referred to as gravity reduction.

The mean value of the gravity at the Earth's surface is about 9.8 ms^{-2} and variations in gravity caused by density variations in the subsurface are of the order of 100 μms^{-2}. The most common parameters used in gravity method are CGS and SIs unit system as shown in the following table:

Table 2.1 Unit system commonly used in gravity method (after Hinze et al., 2013)

Gravity parameters	CGSu	SIu
Gravitational constant	6.674 X 10^{-8} $cm^3/g\ s^2$	6.674 X 10^{-11} $m^3/kg\ s^2$
Force of attraction	10^5 dyns	Newton(N)
Gravitational acceleration	cm/s^2 milliGal (mGal) microGal (μGal)	10^{-2} m/s^2 10^{-5} m/s^2 10^{-8} m/s^2
Density	g/cm^3	10^3 kg/m^3

The measurement of gravity gradients is often given in the Eötvös unit which is equals 10^{-4} mGal/m or 0.1 mGal/km.

2.2 Magnetic method

The magnetic scalar potential $V(r)$, of a dipole whose magnetic moment is **m**, can be written as:

$$V(r) = -\mathbf{m}\bullet\nabla\left(\frac{1}{r}\right), \qquad 2.7$$

where r is the distance operator.

The magnetic field may also be defined in terms of electric currents. If an electric current **I**, is flowing in a loop of radius r, the magnetic strength at the center of the loop is $\mathbf{H}=\mathbf{I}/2r$.

2.2.1 Magnetic Permeability and Susceptibility.

Materials can be magnetized by acquiring the component of magnetization in the presence of an external magnetic field and it is called induced magnetization which is in the same (or reverse) direction of the external magnetic field as:

$$\mathbf{M} = \chi \mathbf{H} \,. \qquad 2.8$$

The constant χ in the Equation 2.9 is called the *magnetic susceptibility*. Susceptibility is a dimensionless quantity but differs in magnitude as it is in emu equals 4π times in SI units.

While *magnetic permeability* μ, is different in both the systems and derived differently as following:

In the emu system,

$$\begin{aligned} \boldsymbol{B} &= \mathbf{H} + 4\pi\mathbf{M} \\ &= \mathbf{H} + 4\pi\chi\mathbf{H} \\ &= (1 + 4\pi\chi)\mathbf{H} \\ &= \mu\mathbf{H} \end{aligned}$$

$$\mu = 1 + 4\pi\chi \,. \qquad 2.9$$

In SI units,

$$\begin{aligned} \boldsymbol{B} &= \mu_0(\mathbf{H} + \mathbf{M}) \\ &= \mu_0(\mathbf{H} + \chi\mathbf{H}) \\ &= \mu_0(1 + \chi)\mathbf{H} \\ &= \mu\mathbf{H} \end{aligned}$$

$$\mu = \mu_0(1 + \chi). \qquad 2.10$$

The relationship between **M** and **H** is not necessarily linear because the magnetic susceptibility χ may vary with the field intensity, may be negative, and may be represented more accurately in some materials as a tensor (Blakely, 1996). Susceptibility is in essence a measure of how susceptible a material is to become magnetized (Reynolds, 1997).

There are many kinds of magnetizations and their understanding is important how the variations of magnetic properties produce the magnetic anomalies (Hinze et al., 2013). These properties can be defined as:

Diamagnetism, for example, is an inherent property of all matter. In the presence of external magnetic field, the orbital path of the electron rotates in a way that induced magnetization is small and in the opposite sense to the applied field. Consequently, diamagnetic susceptibility is negative.

Paramagnetism, is a property of those solids that have atomic magnetic moments because in this substances, the electron shells are incomplete so the unpaired electrons produce a magnetic field. When it is placed in an external magnetic field, the atomic moments or unpaired electrons partially align parallel to the applied field thereby producing a net magnetization in the direction of the applied field. This is still, however a relatively weak effect. However, all minerals are diamagnetic and some are paramagnetic but in both cases their magnetizations do not have significant contributors to the geomagnetic field.

Though, there is a class of magnetism that have great importance on geomagnetic studies. Certain materials not only have atomic moments, but neighboring moments interact strongly with each other. This interaction is a result of a quantum mechanical effect called exchange energy. Suffice it to say that the exchange energy causes a *spontaneous magnetization* that is many times greater than paramagnetic or diamagnetic effects (Blakely, 1996). These types of materials are called *ferromagnetic*. There are several types of ferromagnetic materials, depending on the alignment of their atomic moments. If the atomic moment aligned parallel to one another, results *ferromagnetism*; if the atomic moment aligned antiparallel to one another and total moment is neutralized, results *anti-ferromagnetism*; and the last is the *ferrimagnetism*, in which atomic moments are antiparallel but do not cancel. The strength of the magnetization of *ferromagnetic* and *ferrimagnetic* materials decreases with temperature and disappears at the *Curie temperature* (Kearey et al., 2002).

The *spontaneous magnetization* of ferromagnetic materials can be very large at the scale of individual mineral grain but due to random orientation the net magnetization may be negligible at outcrop scale. Due to the presence of ferromagnetic mineral, rocks will acquire a magnetization $\mathbf{M}_i$, called *induced magnetization* in the direction of applied filed **H** can be denoted as:

$$\mathbf{M_i} = \chi \mathbf{H} .$$

If the rock is placed in a field-free environment, the induced magnetization falls to zero (Blakely, 1996). However, ferromagnetic materials have a special ability to retain a permanent magnetization even in the absence of external magnetic fields and it is called *remanent magnetization*, may be denoted by $\mathbf{M}_r$. The remanent magnetization of crustal rock depends not only on their atomic structure, crystallographic and chemical composition, but also on their geological, tectonic and thermal history. In geophysical studies, it is usual to consider the total magnetization M of the rock as the vector summation of induced and remanent magnetization, that is:

$$\mathbf{M} = \mathbf{M}_i + \mathbf{M}_r = \chi\mathbf{H} + \mathbf{M_r}\,. \qquad 2.11$$

The ratio between remanent magnetization and induced magnetization is expressed by the *Koenigsberger ratio* as the following:

$$Q = \frac{\mathbf{M}_r}{\mathbf{M}_i} = \frac{\mathbf{M}_r}{\chi\mathbf{H}}\,. \qquad 2.12$$

These may be oriented in different directions and may differ significantly in magnitude. The magnetic effects of a rock arise from the resultant **M** of the two magnetization vectors.

Magnetic anomalies caused by the rocks are superposed to the geomagnetic field similar to gravity anomalies which are superposed to the gravitational field. However, the magnetic field is more complex, due to variation in amplitude and in direction of the geomagnetic field. Consequently, knowledge of the behavior of the magnetic field is necessary both in the reduction of magnetic data to a suitable datum and in the interpretation of the resulting anomalies. The magnetic field is geometrically more complex than the gravity field of the Earth and exhibits irregular variation in both orientation and magnitude with latitude, longitude and time (Kearey et al., 2002).

Total-field magnetometers are usually the instrument of choice for airborne and shipborne magnetic surveys. As the name implies, total-field magnetometers measure the magnitude of the total magnetic field without regard to its magnetic direction.

The total field **T** is given by:

$$\mathbf{T} = \mathbf{F} + \Delta\mathbf{F}\,, \qquad 2.13$$

where **F** is the geomagnetic field and $\Delta\mathbf{F}$ represents the perturbation of **F** due to some crustal magnetic sources.

The total-field anomaly is calculated from total-field measurements by subtracting the magnitude of a suitable regional field, usually the IGRF model appropriate for the date of the survey. If **T** represents the total field at any point, and **F** is the regional field at the same point, then the total-field anomaly is given by (Blakely, 1996):

$$\Delta\mathbf{T} = |\mathbf{T}| - |\mathbf{F}|\,. \qquad 2.14$$

If $|\mathbf{F}| >> |\Delta\mathbf{F}|$, the total field $\Delta\mathbf{T}$ can be considered as the component of the anomalous field $\Delta\mathbf{F}$ in the direction of **F** and thus it can be considered a harmonic function (e.g., Blakely, 1996). This condition is usually verified in crustal magnetic studies.

The SI unit of magnetic field strength is the tesla (T). For the magnetic variation due to rock, a subunit, the nanotesla (nT), is commonly used; 1 nT=10^{-9}T. The strength of **F** varies from about 25000 nT in equatorial regions to about 70000 nT at the poles (Kearey et al., 2002).

2.2.2 Poisson's Relation.

The governing laws of the gravitational attraction and magnetic scalar potential have some obvious similarities (e.g. their magnitude are inversely proportional to the squared distance to their point sources). By eliminating this common factor in both the formulas we may provide a relationship that is called *Poisson's relation*:

$$V = \frac{kMg_i}{\gamma\rho}, \qquad 2.15$$

where g_i is the component of gravity in the direction of magnetization, γ is the gravitational, M is the uniform magnetization, ρ the constant density, and $k = \mu_0/4\pi$ henry/meter (where μ_0 is the permeability of free space).

The relation states that the magnetic potential is proportional to the gravitational attraction in the direction of magnetization, provided a common source have uniform magnetization and density distributions (Blakely, 1996).

3 Transformations of potential fields and forward modeling

Transformations of potential fields provide the desired geological information that cannot be retrieved from measured data. There are many transformations applied to potential field data, but here we will discuss only those used in this thesis, such as upward continuation and derivatives.

3.1 Upward continuation of the field

Upward continuation is an operator applied to potential field data to transform the anomaly field measured at some level to that on a higher level. Particularly, upward continuation is a low pass filter as it relatively attenuates the high frequency components of the field, such as the effects caused by the shallowest sources.

Upward continuation originates from Green's third identity (Blakely, 1996), which defines that if U is a harmonic continuous function, with continuous derivatives through a regular region R, then at any point P within the harmonic region R, it can be evaluated from its behavior on the boundary S:

$$U(P) = \frac{1}{4\pi}\int_S \left(\frac{1}{r}\frac{\partial U}{\partial n} - U\frac{\partial}{\partial n}\frac{1}{r}\right) dS\,, \qquad 3.1$$

where n is the outward normal direction, r is the distance from P to the point of integration on S. No information is needed about the sources except that it must be outside of the region R.

Upward continuation can be performed level-to-level, level-to-draped, draped-to-level and draped-to-draped. The simplest and most common case is the level-to-level continuation. In this case, potential field data are measured on a constant surface z_0 and continued to a desired higher altitude surface. Mathematically, it can be defined as:

$$U(x,y,z_0-\Delta z)=\frac{\Delta z}{2\pi}\int_{-\infty-\infty}^{+\infty+\infty}\frac{U(x',y',z_0)}{[(x-x')^2+(y-y')^2+\Delta z]^{3/2}}dx'dy'\,, \qquad 3.2$$

where $\Delta z > 0$, and z is negative outward. Basically, Equation 3.2 is a convolution integral and can be performed using the Fourier transform and the convolution theorem. The numerical implementation of this formula obviously considers a finite-extent and equally spaced dataset, which leads to the known types of errors for the continued data (Fedi et al., 2012; Mastellone et al., 2014). Upward continued data can be calculated either by the convolution in space domain or multiplication in Fourier domain. Therefore, in the frequency domain, the Fourier transform of the data is simply multiplied by the frequency operator:

$$e^{-|\mathbf{k}|\Delta z};\ \ \Delta z>0\,, \qquad 3.3$$

where **k** is the wavenumber vector. In practice, the real dataset is discrete and refers to a finite survey area. Thus, errors may affect the low frequency content, while applying upward continuation in the frequency domain. These errors can be significantly reduced, by extending the dataset by adding data through another survey or by extrapolating the dataset (Fedi and Pilkington, 2012; Oppenheim and Schafer, 1975). Extrapolation of the dataset can be done: zero-padding, symmetric extension (Fedi et al., 2012) or maximum entropy extension (Gibert and Galdéano, 1985).

3.2 Derivatives of the potential field

Both horizontal and vertical derivative of potential field are very useful and significantly contribute to the edge analysis of anomalous sources (Nabighian, 1972; Simpson et al., 1986;). The main purpose of using different orders of the derivatives, is to calculate the scaling function along different ridges (Fedi, 2007; Fedi et al., 2009). In the following chapters, we will discuss the scaling function and multi-ridge method in detail.

Consider a scalar quantity $\phi(x,y)$ measured on the horizontal surface. The *horizontal derivatives* of them can be easily calculated space domain by finite difference method as:

$$\frac{d\phi(x,y)}{dx} \approx \frac{\phi(x+\Delta x,y)-\phi(x,y)}{2\Delta x}. \qquad 3.4$$

$$\frac{d\phi(x,y)}{dy} \approx \frac{\phi(x,y+\Delta y)-\phi(x,y)}{2\Delta y}. \qquad 3.5$$

It is also possible to calculate horizontal derivatives in Fourier domain (e.g. Pedersen, 1989) as:

$$\mathcal{F}\left[\frac{d^n\phi}{dx^n}\right] = (ik_x)^n\mathcal{F}[\phi];\ or, \qquad \mathcal{F}\left[\frac{d^n\phi}{dy^n}\right] = \left(ik_y\right)^n\mathcal{F}[\phi], \qquad 3.6$$

where $(ik_x)^n$ and $(ik_y)^n$ are the filters that transform the field into the n^{th}-order field derivative with respect to x and y.

If we consider ϕ as the potential, it is possible to compute the vertical derivative of the field thanks to the Laplace Equation:

$$\frac{\partial^2\phi}{\partial z^2} = -\frac{\partial^2\phi}{\partial x^2} - \frac{\partial^2\phi}{\partial y^2}, \qquad 3.7$$

which leads to:

$$\mathcal{F}\left[\frac{\partial^2\phi}{\partial z^2}\right] = k_x^2\mathcal{F}[\phi] + k_y^2\mathcal{F}[\phi], \qquad 3.8$$

$$\mathcal{F}\left[\frac{\partial^2\phi}{\partial z^2}\right] = |k|^2\mathcal{F}[\phi]. \qquad 3.9$$

So, by applying the Fourier transform to potential field data, multiplying by $|k|^2$, and then applying the inverse Fourier transformation, the second vertical derivative of the potential can be obtained. This formula can be extended to any n^{th}-order vertical derivative of the potential (Blakely, 1996) as following:

$$\mathcal{F}\left[\frac{\partial^n \phi}{\partial z^n}\right] = |k|^n \mathcal{F}[\phi]\,. \tag{3.10}$$

Now we move to the forward modeling of the anomalous fields. The work developed in this thesis can be applied to any type of potential field data but here, we will show the application only on gravity data. We will discuss in the last chapter about other possible application and extension of the developed method.

In the following section, we will discuss the 2D Talwani's approach and its extension to calculate the derivatives of the field by complex sources.

3.3 2-D modelling of complex sources by Talwani's formula

In order to consider a generic multiple-source body, generating an inhomogeneous field, we here use the gravity field formula due to Talwani for 2D sources (Talwani et al., 1959). Any two-dimensional body can be modeled by approximating its boundary by a polygon with a set of q sides (Figure 3.1). We here follow all the notations given by Blakely, 1996. With this formulation for the source, the gravity field g will be expressed at some arbitrary points $[\bar{x}_i, \bar{z}_i]_{i=1,\dots,L}$ as (Talwani et al., 1959; Blakely, 1996):

$$g_i(x_q z_q) = 2\gamma\rho \sum_{q=1}^{Q} \frac{\beta_q}{1+\alpha_q^2}\left[\log\frac{r_{q+1}}{r_q} - \alpha_q(\theta_{q+1} - \theta_q)\right], \tag{3.11}$$

where γ and ρ are the gravitational constant and density respectively; Q is the number of sides of the polygon; x_q and z_q are the coordinates of the polygon vertices; r_q and θ_q are defined according to Figure 3.1 and following formulas:

$$\alpha_q = \frac{x_{q+1}-x_q}{z_{q+1}-z_q}, \qquad \beta_q = (x_q - \bar{x}_\iota) - \alpha_q (z_q - \bar{z}_\iota).$$

$$r_q = \left[(x_q - \bar{x}_\iota)^2 + (z_q - \bar{z}_\iota)^2\right]^{1/2}.$$

$$r_{q+1} = \left[(x_{q+1} - \bar{x}_\iota)^2 + (z_{q+1} - \bar{z}_\iota)^2\right]^{1/2}.$$

$$\theta_q = \tan^{-1}\left(\frac{z_q - \bar{z}_\iota}{x_q - \bar{x}_\iota}\right).$$

$$\theta_{q+1} = \tan^{-1}\left(\frac{z_{q+1}-\bar{z}_\iota}{x_{q+1}-\bar{x}_\iota}\right).$$

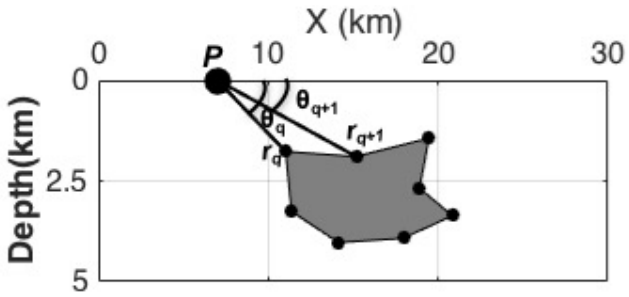

Figure 3.1 A generic complex source.

As in further computation we will perform inversion of the scaling function of high-order derivatives, it is convenient to extend Equation 3.11 for calculating field derivatives.

3.3.1 Talwani's formula for the vertical field derivative (∂g/∂z).

We can simply take the partial derivative of the field in Equation 3.11, in order to extend it for vertical derivative as:

$$\left(\frac{\partial g}{\partial z}\right)_i = 2\gamma\rho \sum_{q=1}^{Q} \left[\left\{ \frac{\alpha_q}{1+\alpha_q^2} \left(\log \frac{r_{q+1}}{r_q} - \alpha_q(\theta_{q+1} - \theta_q) \right) \right\} \right.$$
$$+ \frac{\beta_q}{1+\alpha_q^2} \left\{ \left(\frac{(z_q - \bar{z}_i)}{r_q^2} - \frac{(z_{q+1} - \bar{z}_i)}{r_{q+1}^2} \right) \right. \qquad 3.12$$
$$\left. \left. - \alpha_q \left(\frac{(x_q - \bar{x}_i)}{r_q^2} - \frac{(x_{q+1} - \bar{x}_i)}{r_{q+1}^2} \right) \right\} \right].$$

3.3.2 Talwani's formula for the horizontal field derivative (∂g/∂x).

Similarly, we can extend the Equation 3.11 for calculating the horizontal derivative by taking partial derivative with respect to *x* as following:

$$\left(\frac{\partial g}{\partial x}\right)_i = \sum_{q=1}^{Q} \left[\left\{ \frac{-\alpha_q}{1+\alpha_q^2} \left(\log \frac{r_{q+1}}{r_q} - \alpha_q(\theta_{q+1} - \theta_q) \right) \right\} \right.$$
$$+ \frac{\beta_q}{1+\alpha_q^2} \left\{ \left(\frac{(x_q - \bar{x}_i)}{r_q^2} - \frac{(x_{q+1} - \bar{x}_i)}{r_{q+1}^2} \right) \right. \qquad 3.13$$
$$\left. \left. - \alpha_q \left(\frac{(z_{q+1} - \bar{z}_i)}{r_{q+1}^2} - \frac{(z_q - \bar{z}_i)}{r_q^2} \right) \right\} \right].$$

The formula given in Equation 3.11 is also derived for higher orders of derivatives, which are given in Appendix A. In further chapters, we will see that these formulas are needed in order to calculate the scaling function and so define the objective function for the inverse problem.

The gravity field and its derivatives can be numerically calculated by assigning values to the coordinates of the vertices, as shown in Figure 3.2 for the source described in Figure 3.1, assuming a 1 g/cm^3 density contrast.

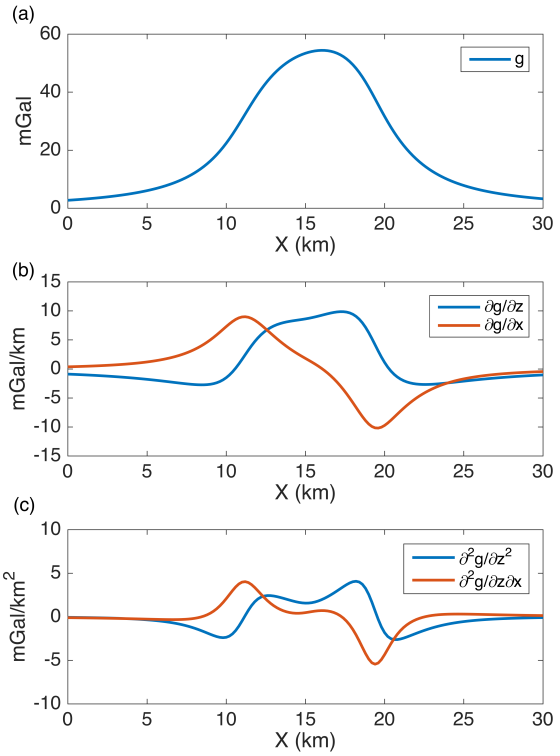

Figure 3.2 a) Gravity field (g) due to the complex source given in Figure 3.1; b) ∂g/∂x and ∂g/∂z; c) ∂²g/∂z²and ∂²g/∂z∂x;

4 Multi-Homogeneity Depth Estimation (MHODE)

Fedi et al., (2015) developed a method for estimating the source-parameter from homogeneous or inhomogeneous potential field data, called Multi-Homogeneity Depth Estimation (MHODE). They proposed the generalization of the homogeneity law into a multi-homogeneity law, accounting for the fact that the homogeneity degree is a scale dependent quantity that changes with respect to the distance from the sources, except in the asymptotic regions. These asymptotic regions may occur when the observation point is either very near to the source or very far to the source. However, in practical world we basically study the field somewhere between these two regions and deal with inhomogeneous field. Therefore, the MHODE method allows studying inhomogeneous potential fields.

The MHODE method involves the inversion of the scaling function (Fedi, 2007) of the potential field in a multiscale framework. The practical approach of the MHODE methods includes the following steps: a) upward continuation of the field in 3D space; b) Multi-ridge analysis of continued field; c) calculation of the scaling function along the ridges; d) forming a system of equations for the scaling function (this means that we approximate the inhomogeneous field to be locally homogeneous at each altitude); e) solving the system of equations to retrieve the unknown source parameters.

In the further section, before discussing the main theoretical aspect of MHODE method, we will briefly discuss about multi-ridge analysis of potential field, scaling function and Depth from Extreme Points (DEXP, Fedi, 2007) methods, as the theoretical root of the scaling function lies in the DEXP theory.

4.1 Multiridge method

The Multiridge method (Fedi et al., 2009) is a geometrical method to find the source depth by searching the intersection of different ridges in the source region. As the name of the method suggests, this is a multiscale method that use the homogeneity law and the upward continuation of the potential field in the 3D space. It allows estimating

the source position in a very easy way. More precisely, the method is based on the evaluation of the zeroes of the absolute values of the horizontal derivative of the field (called ridges) at a set of altitudes.

Potential fields of simple or ideal sources are homogeneous functions of degree *n:*

$$f(tx, ty, tz) = t^n f(x, y, z)\,. \qquad 4.1$$

For many kinds of ideal sources, the homogeneity degree corresponds to the fall-rate of the field (Thompson, 1982). The homogeneity degree n may be written as $n = v\text{-}p$, where v is an integer value ranging from 0 to 3, depending on the kind of homogeneous source (i.e. sphere, cylinder, dike and contact) and p is the order of the potential field (i.e. magnetic, $p = 3$; gravity, $p = 2$ etc.). For instance, for the magnetic field of a homogeneously magnetized sphere, $n = -3$, $p = 3$, and $v = 0$ (Fedi et al., 2009).

Fedi et al., 2009 gave a quite extended definition of ridges, defining three types of ridges:

- Zeros of the horizontal derivative
- Zeros of the vertical derivative
- Zeros of the field itself

Generally, the computed ridges are straight lines for homogeneous or one-point sources (Fedi et al., 2009) and the intersection of the ridges occurs in the source region at the source position (i.e. at the depth to the center of a sphere or at the depth to the top of an infinite vertical cylinder). However, if the field is not homogeneous, as it trivially occurs in the case of interfering anomalies, the computed ridges are curved (Fedi et al., 2009). The number of ridges depends on the order of the partial derivatives of the field, it increases according to the order of the field.

There are several approaches to draw the ridges automatically by computer algorithm, by searching for the zeros or the maxima/minima of a function. As proposed by Fedi et al., (2009), Canny's algorithm (1986) is one of the more efficient algorithm, which allows to search for maxima/minima of a generic function F. If $F(x,y)$ is a function

and $\partial F/\partial x$ and $\partial F/\partial z$ are its gradients. Canny's (1986) algorithm searches for the maxima and minima of F as the points where Mf is locally maximum in the Af direction, where:

$$Mf = \sqrt{\left(\frac{\partial F}{\partial x}\right)^2 + \left(\frac{\partial F}{\partial y}\right)^2}, \tag{4.2}$$

and

$$Af = \tan^{-1}\left(\frac{\partial F}{\partial y} \Big/ \frac{\partial F}{\partial x}\right). \tag{4.3}$$

First, extreme points are calculated at each altitudes and, then, ridges are obtained by joining each extreme point at a given altitude to the nearest one computed at the altitude just above.

Fedi et al., (2009), demonstrated the validity of the method for the magnetic field but the same is valid for any other type of potential field, such as the gravity one.

The magnetic field at a point $P_1(x,y,z)$, due to the magnetic dipole at a point $P_2(x_0,y_0,z_0)$ can be written as follows considering the Cartesian coordinates system with the z-axis directed downward:

$$F_3 = C_m \mathbf{f} \cdot \nabla \left[\mathbf{t} \cdot \boldsymbol{\nabla} \frac{|\mathbf{M}|}{\|\boldsymbol{r} - \boldsymbol{r}_0\|_2}\right], \tag{4.4}$$

where $\boldsymbol{r}$ and $\boldsymbol{r}_0$ are the position vectors relative to the points P_1 and P_2 respectively, $\mathbf{M}$ is the sphere dipole moment, $C_m = \mu_0 / 4\pi$, μ_0 is the permeability of the free space, $\mathbf{f}$ is the unit vector in the local direction of the geomagnetic field $\mathbf{H}$, $\mathbf{t}$ is the unit vector along the direction of $\mathbf{M}$ and $\boldsymbol{\nabla}$ is the gradient operator vector. The order of the potential field p, is three.

As already mentioned, there are three type of ridges, defined by Fedi et al., (2009): a) type I, zeros of the horizontal derivative of the potential field; b) type II, zeros of the vertical derivate of the potential field; and c) type III, zeros of the potential field itself. The first type of ridge of the magnetic field in Equation 4.4 can be obtained by the

computing the horizontal derivative of F_3, considering the cross section $y = y_0$, and $|\mathbf{M}| = 1$:

$$\frac{\partial F_3(r, r_0)}{\partial x} = C_m \left(\frac{\begin{matrix}(X^3 + XZ^2)t_y f_y + (3XZ^2 - 2X^3)t_x f_x + (Z^3 - 4X^2Z)t_z f_x \\ +(Z^3 - 4ZX^2)t_x f_z + (X^3 - 4XZ^2)t_z f_z\end{matrix}}{(X^2 - Z^2)^{7/2}} \right), \quad 4.5$$

where $X=x-x_0$ and $Z=z-z_0$.

From this equation we can see that the ridges are straight lines, which can be expressed as:

$$x - x_0 = \beta(z - z_0)\,, \quad 4.6$$

where $\beta = \tan(\phi)$ and ϕ is the angle between a ridge and vertical axis z. If we assume that inclination and declination of the geomagnetic field are 0° and 90°, respectively, and **f**=**t**, the solution of the Equation 4.5 is:

$$\begin{aligned} x &= x_0\,, \\ x - x_0 &= 2(z - z_0)\,, \\ x - x_0 &= -2(z - z_0)\,. \end{aligned} \quad 4.7$$

These three solutions (Equation 4.7) are the straight lines intersecting at the center of the sphere (x_0, z_0). This demonstration proves mathematically the validity of the method. It can be done in a similar manner for the vertical derivative or for higher order derivatives of the field.

As mentioned before, the method can be applied to any potential field. Figure 4.1 shows the application to gravity anomaly produced by a sphere of radius 1 km situated at a 6 km depth. The field is computed up to 10 km altitude in *x*-*z* plane and ridges are computed according to above description of the method. Ridges are joining in the source region at the depth of 6 km, which is the same depth of the center of the assumed sphere.

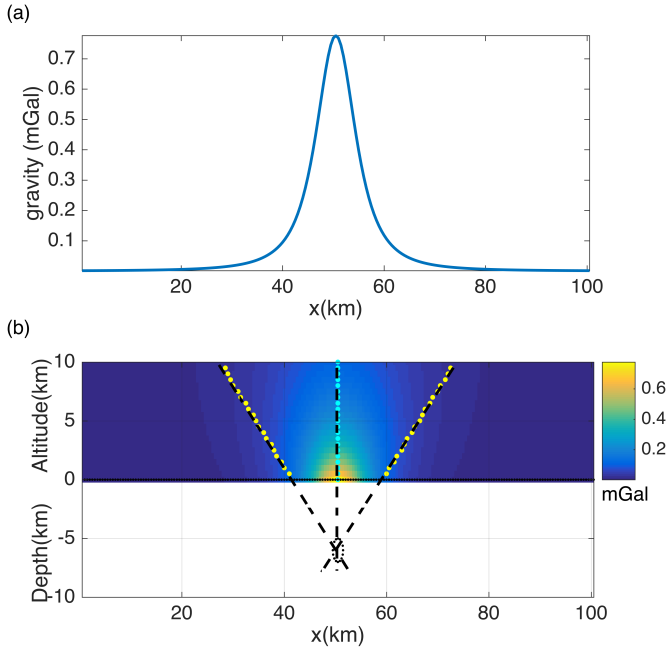

Figure 4.1 Depth estimation by multiridge method. a) gravity anomaly by a sphere with density contrast of 1 g/cm^3; b) data is computed up to 10 km and ridges joining in the source region at 6 km depth.

4.2 DEXP method and Scaling function

The Depth from Extreme Points (DEXP) method is an imaging method to retrieve the three-dimensional position of the source from potential field data. The method was developed by Fedi, 2007. Particularly, the method works in a semi-automatic way, like Euler deconvolution method, to estimate the source position and characteristic parameter of the source (Structural Index, Reid et al., 1990).

The DEXP method can be applied to any potential field and its derivatives and the method is also very stable vs. noise. The DEXP method can be applied to potential field using following step:

- *Upward continuation of the field*: DEXP requires that the data, horizontally and vertically in 3D space. So it is necessary to create a 3D data volume of the potential field.

- *Scaling of the field*: Any field $f(r, r_0)$ has to be scaled using specific laws. If the field is originated by a source at r_0, it is transformed into a scaled field $W(r, r_0)$.
- *Estimation of the source depth:* This step involves determining the position of the source by searching the extreme points of the scaled field. The extreme points will occur for the scaled field $W(r, r_0)$ at $r(x,y,z)$ that is symmetrical to the $r_0(x_0,y_0,z_0)$, with respect to the vertical axis.
- *Calculation* of excess mass in gravity or excess dipole moment intensity for the magnetic field.

The mathematical derivation of the DEXP method is given by following the demonstration of the Fedi, 2007. Consider the Newtonian potential and its derivatives of degree *n*:

$$f(\mathbf{r}) = k\frac{\partial^n}{\partial z^n}\int_V \frac{M(\mathbf{r_0})}{\|\mathbf{r}-\mathbf{r_0}\|_2} d^3\mathbf{r_0}\,, \tag{4.8}$$

where k is the physical constant related to field, M is the source density, and $\mathbf{r}$ and $\mathbf{r_0}$ are the position vectors of the observation and source respectively.

Let us consider the gravity field $f_1(\mathbf{r})$ due to a single pole at the point $\mathbf{r_0}(x_0,y_0,z_0)$ with the density M. It can be written as follows:

$$f_1(\mathbf{r}) = M\frac{(z-z_0)}{\|\mathbf{r}-\mathbf{r_0}\|_2^3}. \tag{4.9}$$

If we assume a unit density, the source at $\mathbf{r_0}(0,0,z_0)$ and the field at $x= x_0$, $y= y_0$, Equation 4.9 will be:

$$f_1(z) = \frac{1}{(z-z_0)^2}. \tag{4.10}$$

Fedi, 2007 defined the **scaling function** τ, by the derivative of the logarithm of the field f with respect to log(z) as:

$$\tau(z) = \frac{\partial \log[f(z)]}{\partial \log(z)}. \qquad 4.11$$

The scaling function τ_1 of f_1 is then:

$$\tau_1(z) = -\frac{2z}{z - z_0}. \qquad 4.12$$

We can see from Equation 4.12 that τ_1 has a singularity at $z = z_0$, that is in the source region. However, at $z = -z_0$:

$$\tau_{1(z=-z_0)} = -\frac{-2z_0}{-z_0 - z_0} = -1. \qquad 4.13$$

It follows that,

$$\frac{\partial\{\log[f_1(z)] + \log(z)\}}{\partial z}\Big|_{z=-z_0} = 0. \qquad 4.14$$

This can be written as:

$$\frac{\partial z f_1}{\partial z}\Big|_{z=-z_0} = 0. \qquad 4.15$$

The function zf_1 has the maxima at $z = -z_0$. The scaled gravity field is W_g:

$$W_{g1} = f_1 z, \qquad 4.16$$

has its maximum at $x = x_0$, $y = y_0$ and $z = -z_0$. This maximum occurs when a positive density contrast is assumed, while the minimum occurs in case of a negative density contrast.

Fedi, (2007) generalized the formula to any p^{th} order of vertical derivative of the field, f_p and to any type of homogeneous source. Starting from p^{th} order derivative of gravity field having homogeneity degree n, $f_p(x = x_0, y = y_0, z) = \frac{1}{(z-z_0)^{N+p}}$, where N= -n. So the scaling function for p^{th} order is:

$$\tau_p = \frac{\partial \log[f_p]}{\partial \log(z)} = -\frac{(N+p)z}{(z-z_0)}. \qquad 4.17$$

At z= -z_0, this can be written as:

$$\tau_p(z = -z_0) = -\frac{N+p}{2}. \qquad 4.18$$

Hence, the general scaled function W_p

$$W_p = f_p z^{N+p/2}, \qquad 4.19$$

have extreme points at (x= x_0, y= y_0, z= -z_0).

So, Equation 4.19 is the general form of the scaling function that is valid for any homogeneous potential field or any of its derivatives.

In this thesis, the scaling function will play a key role since it does not depend on the physical property, namely the density for the gravity field and its derivatives. Equation 4.11 and Equation 4.17 will be so used throughout this thesis.

Figure 4.2 presents an application of the DEXP method about a simple case of gravity field due to a sphere situated at 8 km depth. As it is shown in Figure 4.2, DEXP is applied on the first vertical derivative of the gravity field and allows the exact depth of the sphere to be estimated (white plus sign on Figure 4.2d). For the advanced development and more details on the application of DEXP and scaling function, readers are referred to other papers such as, Fedi, (2007); Fedi and Pilkington, (2012); Fedi and Florio, (2013); Abbas et al., (2014); Abbas and Fedi, (2014); Baniamerian et al., (2016).

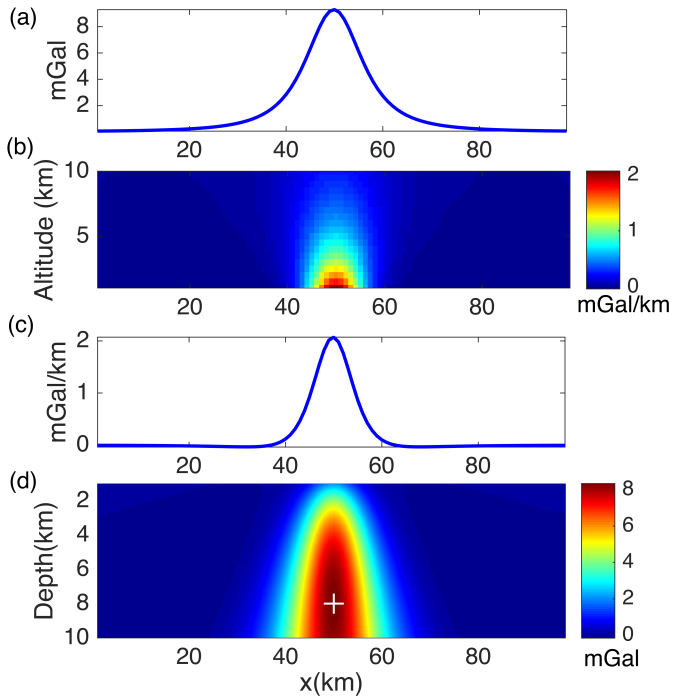

Figure 4.2 DEXP is applied on the gravity field over a buried sphere.

4.3 Theory of MHODE method

We will briefly describe here the Multi-HOmogeneity Depth Estimation (MHODE) method, allowing studying homogeneous and inhomogeneous potential fields as well.

Considering the framework of homogeneous fields, there are many automatic methods proposed for interpreting the potential fields, such as those based on the Euler deconvolution (e.g., Thompson, 1982; Reid et al., 1990; Ravat, 1996; Fedi et al., 2009), the local wavenumber (e.g., Thurston and Smith, 1997; Smith et al., 1998), the Continuous Wavelet Transform (CWT) (e.g., Moreau et al., 1997; Fedi et al., 2010; Fedi and Cascone, 2011), the Depth from Extreme Point (DEXP) (Fedi, 2007; Fedi and Pilkington, 2012; Fedi and Florio, 2013; Abbas et al., 2014; Abbas & Fedi, 2014; Baniamerian et al., 2016) and the Multi-ridge Method (Fedi et al., 2009; Florio and Fedi, 2014). All these methods are developed assuming that the field is homogeneous at least locally, i.e. within a moving window. More precisely, the best homogeneous field is searched for each position of the moving window, which can fit measurements therein.

Homogeneous potential fields *f,* are generated by ideal homogenous sources and satisfy the homogeneity law (Equation 4.1) or, equivalently, the Euler's differential homogeneity equation:

$$\frac{\partial f}{\partial x}(x-x_0)+\frac{\partial f}{\partial y}(y-y_0)+\frac{\partial f}{\partial z}(z-z_0)=-nf\ , \qquad 4.20$$

where n is the homogeneity degree, t>0 and $\{x_0, y_0, z_0\}$ are the coordinates of the unknown single source.

Here, the potential field f is generated by one point sources and the source distribution of such sources may be defined by a single point. The best example of this kind of sources is the homogeneously dense sphere whose field is equivalent to that of a point-mass having its mass distribution concentrated on its center, so that the gravity field may be defined by this single point (e.g., Fedi, 2016). Other examples are the infinitely extended cylinder in gravity fields, the dipole for magnetic fields, infinitely extended pole and dipole lines, semi-infinitely extended tabular sources, and the semi-infinite block model that may represent contact-like geological structures (e.g., Fedi, 2016). These sources can be interpreted by finding one depth point only (i.e., top of the vertical infinite cylinder in gravity) because their field is equivalent to sources having their mass (or dipole moment in magnetic case) concentrated at that point.

The homogeneity degree n, for such homogeneous sources or one-point sources is the integer values $\{-3, -2, -1, 0\}$. All the methods for interpreting homogeneous fields assume the homogeneity degree as an integer value at least within a local set of data points. However, Fedi et al. (2015) argue that any inhomogeneous field can be homogeneous in two asymptotical conditions, either, a) the measurement point is very near to the source region, so horizontal extension can be approximated to infinite, or b) the measurement point is very far from source region, so any types of sources behave like a point source and the homogeneity degree tends to -3 in magnetic case or -2 in gravity case.

However, in the real world the causative sources are complex sources and measured fields are no more homogeneous fields. Furthermore, Steenland (1968) has shown that

the homogeneity degree *n* is a function of distance for a complex source, and that it may hold fractional values as well. This is confirmed by other authors, dealing with sources which are not one point sources and whose homogeneity degree *n* is fractional: in that case, the retrieved depth is somewhere between the source top and centre (Keating and Pilkington, 2004; Gerovska et al., 2005).

Fedi et al., 2015 treated the problem in a different way, by generalizing the homogeneity law, similar to multifractal scaling laws from monofractals and redefined the Equation 4.1 in following manner:

$$f(ax, ay, az) = a^{n(x,y,z)} f(x, y, z)\,, \tag{4.21}$$

so now Euler differential becomes:

$$\frac{\partial f}{\partial x}(x - x_0) + \frac{\partial f}{\partial y}(y - y_0) + \frac{\partial f}{\partial z}(z - z_0) = -n(x, y, z) f(x, y, z)\,, \tag{4.22}$$

where now, *n* is a function of distance to the source and *f* is an inhomogeneous field.

In the further section we will discuss about local homogeneity and multi-homogeneity of the inhomogeneous fields.

4.3.1 Inhomogeneous and Multi-homogeneous fields.

Inhomogeneous fields are fields generated by non-concentrated sources, which cannot be represented by a single one point. In general, these sources are finite in all extent and we may also refer to them as multiple or multipoint sources. Fedi et al., 2015 have shown that any type of field homogenous or inhomogeneous may have integer or fractional values of the homogeneity degree and that it changes with respect to distance from the source. As it can be seen evidently (Figure 4.3) from the example of many sources (Fedi et al., 2015; Ravat, 1994; Steenland, 1968), the estimated homogeneity degree *n*, is varying from 0 to -2 with respect to the depth to the top of the source. So, in

the case of a single-scale study, the homogeneity degree may occasionally assume an integer value but in reality it is continuously tending from 0 to a constant value at higher distance. For instance, the gravity field due to circular disk is representing three ideal sources at different levels: 0 at the lowest distance, where it can be interpreted as a thin sheet, -1 at 0.8 km, where it can be interpreted as a cylindrical structure and -2 at more than 8 km, where it can be interpreted as a pole source (Fedi et al., 2015). The ambiguity of the problem is evident from this example.

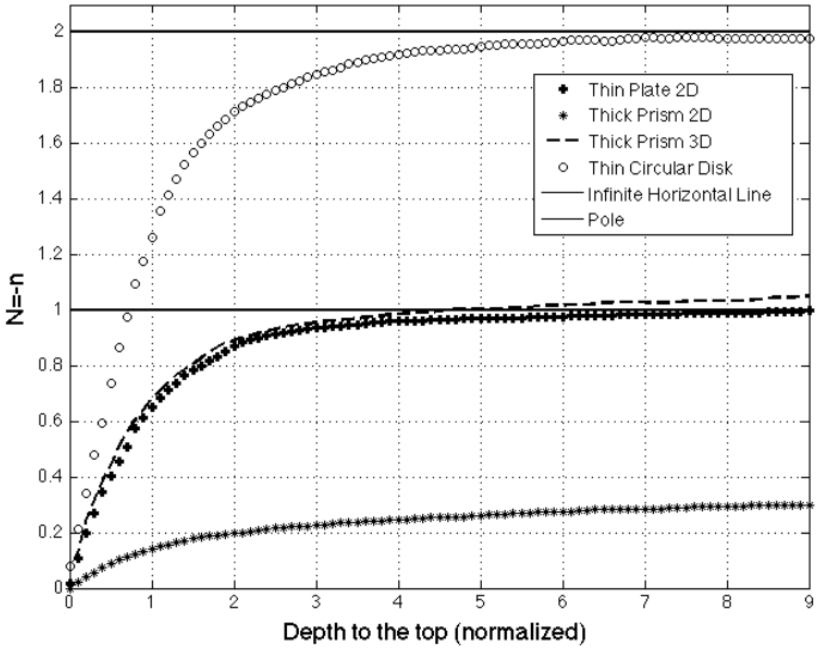

Figure 4.3 The homogeneity degree (n) of inhomogeneous fields versus altitude. Constant curves are related to one point sources. For inhomogeneous sources, the homogeneity degree canges versus the altitude and its fractional. (From Fedi et al., 2015, after Steenland 1968).

Therefore, to study the realistic nature of the sources, real and varying values of the homogeneity degree should be adopted along the whole multiscale dataset. This is similar to multifractals that are also studied at different scales. Fedi et al., (2015) then defined the local homogeneity by distinguishing homogenous and locally homogeneous functions.

Consider $f(\mathbf{r})$ is a continuously differentiable in the region R, then it is locally homogeneous of degree n, if and only if:

$$\nabla f(\mathbf{r})(\mathbf{r}-\mathbf{r}_0) = -nf(\mathbf{r})\,. \qquad 4.23$$

From Equation 4.23 it follows that: (a) $f(\mathbf{r})$ is locally homogeneous of degree n in a region R if and only if f it is homogeneous of degree n in some neighborhood of every point of R; and (b) a locally homogeneous field may be or may not be homogenous, the but reverse is always true.

Since the homogeneity degree is different in different domains of the space, Fedi et al., (2015) introduced a new term for such potential fields, called *multi-homogeneous field*.

So following the concept of multi-homogeneity, any function can be approximated as:

$$f(\mathbf{r}) \sim F_H(\mathbf{r})\,, \qquad 4.24$$

where $F_H(\mathbf{r})$ is the best homogeneous field of degree n along the lines called ridges (Fedi et al., 2009; Fedi et al., 2015; Florio and Fedi, 2014).

4.3.2 Depth estimation of multi-homogeneous model

In this section, we will see the practical approach of the multi-homogeneity theory. We may now explore the scaling function, defined in Equation 4.11. The scaling function has the following expression for ideal sources:

$$\tau(z) = n\frac{z}{z-z_0}, \qquad 4.25$$

where z is the altitude, z_0 is the source depth and n is the homogeneity degree. Using the definition of local homogeneity (Equation 4.24), we can write:

$$\tau(f) \sim \tau[F_H] \quad \forall \mathbf{r} \in W\,, \tag{4.26}$$

where,

$$\tau(f) = \frac{\partial \log(f)}{\partial \log(z)}; \quad \tau[F_H] = n(z)\frac{z}{z - z_0(z)}, \tag{4.27}$$

4.3.3 Depth estimation of complex sources.

We have seen the theoretical development of MHODE method in above sections. Fedi et al., (2015) applied the method to two-point sources such as the finite vertical cylinder and faults. In the next section we will discuss the extension of this approach for more complex and irregular sources, this being the major development of this thesis.

In a real geological scenario, we expect the source distributions are irregular and complex. In particular, we will face the 2D case of gravity. We have already discussed in section 3.3 in chapter 3 the forward formulation to calculate the gravity using Talwani's 2D formula and its extension to calculate higher orders of derivatives of the gravity field. The main goal of this thesis is to invert the scaling function (Equation 4.11), not the field, and so enjoying the advantage of its independence on density or any other physical constant. Note that the scaling function mathematically is only function of the geometrical parameters of the anomalous sources.

Now we may rewrite the formula of the scaling function as:

$$\tau_{T(p)} = \frac{\partial \log(g_p)}{\partial \log(z)}, \tag{4.28}$$

where z is the altitude, g_p is the gravity field or its any p^{th} order of derivatives and $\tau_{T(p)}$, is the respective scaling function where the 'T' subscript refers to some mathematical expression for the scaling function, such as that based on the Talwani's

formula. In order to compute such theoretical expression, we may rewrite Equation 4.28 as following:

$$\tau_{T(p)} = \frac{1}{g_p}\frac{\partial g_p}{\partial z} z \,. \qquad 4.29$$

As it can be seen from Equation 4.29, in order to calculate the scaling function for the field or its derivatives, we need to compute first $\partial g_p / \partial z$.

Now consider first p=0 so that Equation 4.29 is:

$$\tau_T = \frac{\partial \log(g)}{\partial \log(z)} = \frac{1}{g}\frac{\partial g}{\partial z} z \,, \qquad 4.30$$

where g and $\partial g / \partial z$, can be calculated according to Equations 3.11 and 3.12, respectively, as defined in Chapter 3. Similar considerations may be made for computing the scaling function of order $p>1$: we must compute the expression of the $(p+1)^{th}$ order vertical derivatives of the gravity field. Formulas for p=1 and p=2 are described in Appendix A.

Now we may need form a system of equations based on Equations 4.29, in order to calculate the unknown quantities, namely the coordinates of the Q vertices of the polygon, using the Talwani's 2D polygon approach, that is $\{x_q, z_q\}$, as shown in Figure 3.1. We form finally the following system of nonlinear equations along the ridges:

$$\begin{bmatrix} \tau_T(\bar{x}_1, \bar{z}_1, x_1, .., x_q, z_1, .., z_q) = \tau(\bar{x}_1, \bar{z}_1) \\ \dots \qquad\qquad\qquad\qquad\qquad\qquad \dots \\ \tau_T(\bar{x}_i, \bar{z}_i, x_1, .., x_q, z_1, .., z_q) = \tau(\bar{x}_i, \bar{z}_i) \\ \dots \qquad\qquad\qquad\qquad\qquad\qquad \dots \\ \tau_T(\bar{x}_L, \bar{z}_L, x_1, .., x_q, z_1, .., z_q) = \tau(\bar{x}_L, \bar{z}_L) \end{bmatrix} \qquad 4.31$$

where: $\tau(\bar{x}_i, \bar{z}_i)_{i=1,\dots,L}$ refers to the scaling function estimated at points of coordinates $(\bar{x}_i, \bar{z}_i)_{i=1,\dots,L}$ along the ridge and τ_T refers to the theoretical expression of

scaling function. Once again, note that system in Equation 4.31 is independent on the density, as it is based on the scaling function.

In the next chapter, a detailed description will be given for the inversion that is used to solve the system of Equation 4.31.

5 Potential field data inversion

In inversion, a theoretical geophysical response is calculated using assumed model parameters and estimated parameters. This is then compared with the observed data and their misfit is calculated. The process is repeated until the values of the estimated parameters will decrease the misfit adequately (e.g., Dimri, 1992).

The initial task in most geophysical inverse problems is to describe the data. Since, geophysical data are recorded digitally, the dataset is simply a table of numerical values and can be represented by a vector in case of 1D dataset or by a matrix in case of 2D or 3D datasets. For the convenience, considering a vector representation of the data of length N and as well of model parameters of length M (Menke, 1989) as:

$$\mathbf{d} = [d_1, d_2, d_3, \dots, d_N]^T , \tag{5.1}$$

$$\mathbf{m} = [m_1, m_2, m_3, \dots, m_M]^T . \tag{5.2}$$

If the data **d** and model parameter **m** are linearly related to each other, the forward problem can be written in the following form:

$$\mathbf{d} = \mathbf{Am} , \tag{5.3}$$

where **A** the the matrix of (N x M) dimension, is called kernel. Equation 5.3 forms the foundation of discrete linear inverse theory. Many important inverse problems that arise in the physical sciences involve precisely this equation. Others, while involving more complicated, nonlinear, equations, can often be solved through linear approximations (Menke, 1989).

When the length of data N, is greater than the length of the model parameters M, (N>M), the problem is called *overdetermined*. The most straightforward and common way to invert the system is to find so called least-square solution (Menke, 1989), which can be written as:

$$\mathbf{m} = [\mathbf{A}^{\mathrm{T}}\mathbf{A}]^{-1}\mathbf{A}^{\mathrm{T}}\mathbf{d}\,, \tag{5.4}$$

where superscript "T" is representing the transpose of the matrix.

When the number of data points is less than the number of model parameters ($N<M$), the problem is *undetermined* and a common, but not always satisfying, solution of such problem is called the minimum length solution:

$$\mathbf{m} = \mathbf{A}^{\mathrm{T}}[\mathbf{A}\mathbf{A}^{\mathrm{T}}]^{-1}\mathbf{d}\,. \tag{5.5}$$

A common tool used in the inversion is the conjugate gradient (CG): when the dimension of matrix **A** is very large, CG algorithm can be efficiently used because we never form explicitly the matrix $\mathbf{A}^{\mathbf{T}}\mathbf{A}$ or $\mathbf{A}\mathbf{A}^{\mathbf{T}}$, instead requires only the matrix-vector product of type **Ap** and $\mathbf{A}^{\mathbf{T}}\mathbf{q}$ where **p** and **q** are some vectors with dimension of M and N respectively.

The total error E can be defined by sum of squares of the individual error as:

$$E = \sum_{i=1}^{N} e_i^2\,. \tag{5.6}$$

This is the squared Euclidean length of the vector $\mathbf{e}^{\mathbf{T}}\mathbf{e}$. The Euclidean length is one of the possible way to quantifying the size or length of a vector. In general, the norm is used to refer for measuring the length and indicated by a set of double vertical bars: $\|\mathbf{e}\|$ is the norm of vector **e** (Menke, 1989). A general norm L_p (e.g., Menke, 1989; Dimri, 1992; Sen and Stoffa, 2013) is defined as:

$$L_p\ norm\colon\ \|e\|_p = \left[\sum_{i=1}^{N}|e_i|^p\right]^{1/p}\,, \tag{5.7}$$

where N is the number of data points. In geophysical application, the L_2 norm is commonly used, as given by:

$$L_2\ norm:\ \|e\|_2 = \left[\sum_{i=1}^{N} |e_i|^2\right]^{1/2}. \qquad 5.8$$

Use of other norms, e.g. L_1 can also be found in the geophysical literature.

Geophysical problems are often non-linear and the error function can have multiple minima of various size, as shown in Figure 5.1 (Sen and Stoffa, 2013). In these case, we must distinguish among local optimization algorithms and global optimization algorithms (Dimri, 1992; Sen and Stoffa, 2013). Local optimization algorithms generally calculate the gradient of the problem and typically attempt to find a local minimum in the close neighborhood of the starting solution. These types of algorithm are often called greedy algorithm due to their attempt to go downhill.

Global optimization methods attempt instead to find the global minimum of the error function. As described by Sen and Stoffa (2013), these types of algorithms are stochastic in nature and use global information about the error surface to update their current position. However, the convergence of these methods to the globally optimal solution is not guaranteed for all the algorithms except some, those based on simulated annealing under certain conditions. In many cases, global optimization algorithms are still able to find the good solution starting with poor initial models. Global optimization algorithms include genetic algorithm, simulated annealing algorithms and others.

In this thesis, we used the Very Fast Annealing Algorithm (VFSA) for optimizing our problem. In the next section, we will discuss the VFSA and its application to the MHODE method.

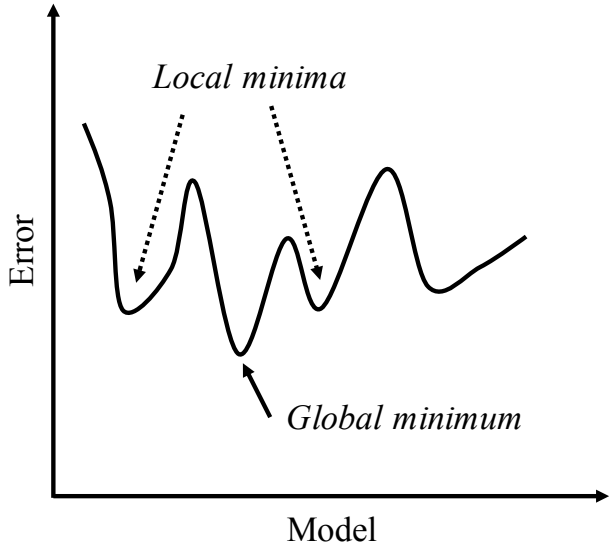

Figure 5.1 Error function showing multiple minima.

5.1 Global optimization for MHODE method

The mathematical formulation of the MHODE problem concerns a set of non-linear equations, which we need to solve using the data at many altitudes. The ultimate goal is to search the source parameters related to the unknown source geometry. The chance to get a good solution to the problem depends on the degree of non-linearity present in the forward problem. In general, more are the sides of the polygon to approximate the geological complex structure, more accurate will be the gravity field computation; however, the inverse problem will become harder to be solved.

To overcome this difficulty, it is possible to get a priori information on some of the vertices of the source by independent information such as geology, wells or other geophysical data. For instance, a salt dome structure is generally poorly defined by a seismic image, except the top-salt. So, gravity is often used to investigate the edges and bottom part of the causative body, while constraining the top part of the body from seismic information. In the next chapter, we will approach this important exploration problem, by assuming the depth to the top known from seismic data and thereafter inverting the data for estimating the edge and bottom part with our method. Our method

can contribute to deal with the complexity of this problem, since it has the advantage of not depending on any a priori information about density.

We will solve Equation 4.31 by using a Very Fast Simulated Annealing method. As discussed above that MHODE involves the inversion of the scaling function so we can write the error function as following:

$$E = \sum (\tau_T - \tau)^2 , \qquad 5.9$$

where τ_T is the theoretical scaling function value computed using the estimated source model and τ is the scaling function evaluated along the ridges.

5.1.1 Very Fast Simulated Annealing

Very Fast Simulated Annealing (VFSA) is the modified version of simulated annealing (SA), proposed by Ingber (1989) who called it very fast simulated re-annealing (VFSR).

Conceptually, SA is extension of statistical mechanics casted in the form of an optimization problem. It is basically a Monte Carlo approach for minimizing a function of large number of parameters (Srivastava and Sen, 2009). Simulated annealing is analogous to the annealing of solid materials and its concept lies in the process of annealing in thermodynamics (Kirkpatrick et al., 1983; Sen and Stoffa, 2013). A physical annealing process occurs when a solid material is heated beyond its melting point and then cooled it down. As molten material goes through different states to cool down or to reach the equilibrium state. The different stages of the cooling process may be referred to the *state*. The probability of any state (say i^{th}) with energy E_i, is given by Gibbs probability density function (or Boltzmann pdf) as follows:

$$P(E_i) = \frac{\exp\left(-\frac{E_i}{KT}\right)}{\sum_{j \in S} \exp\left(-\frac{E_j}{KT}\right)} = \frac{1}{Z(T)} \exp\left(-\frac{E_i}{KT}\right) , \qquad 5.10$$

where S is the set of all the possible configurations, K is the Boltzmann's constant, T is the temperature, and $Z(T)$ is the partition function:

$$Z(T) = \sum_{j \in S} \exp\left(-\frac{E_j}{KT}\right) \quad . \tag{5.11}$$

The main state of this process is the equilibrium state. If the process is cooled down very rapidly (quenching), it will be addressed toward one of the local minima. If, instead, the process is approaching the equilibrium slowly (annealing), it will go close to the global minimum of E (Sen and Stoffa, 2013).

However, the model acceptance criteria of VFSA is the same as used in SA but it differs in the following counts, which makes it more robust and faster.

- Each model parameter in NM dimensional space can have different finite range of variations. Therefore, they are allowed to have different degree of perturbation from their current position.
- Different temperature may be given for each mode parameters but it also required a global temperature for acceptance criteria and this can be different from model parameter temperature.
- The algorithm is very quick to calculate as NM-dimensional Cauchy random generator (Ingber, 1993; Sen and Stoffa, 2013).

To achieve above conditions, VFSA uses following formula for model perturbation:

$$m_i^{k+1} = k_i^k + y_i\left(m_i^{max} - m_i^{min}\right), \tag{5.12}$$

$$y_i = sgn(u_i - 0.5)T_i\left[\left(1 + \frac{1}{T_i}\right)^{|2u_i - 1|} - 1\right], \tag{5.13}$$

with the following cooling schedule:

$$T_i(k) = T_0 \exp\left(-c_i k^{1/NM}\right), \qquad 5.14$$

where m_i^k is the model parameter at the kth iteration, u is a random number between [0,1], T_0 is the global temperature, T_i is the temperature of the *i-th* parameter in the *k-th* iteration and c_i is the decay parameter.

In our case, we are interested to find the model parameters (coordinates of vertices) or state of the process that have the minimum error. VFSA algorithm involves the selection of the new model as being temperature-dependent and the generation of the current model as being based on a Cauchy-like distribution. Cauchy distribution is a continuous probability distribution having an undefined mean. It is also a function of temperature as described by Sen and Stoffa, (1995), therefore the shape of the distribution is controlled by changing the temperature T.

The algorithm starts with a starting random model m_0 with initial temperature T and corresponding energy $E(m_0)$. A search range is required for each model parameter (called bounds). Then the algorithm works iteratively and at each iteration it generates a new random model (say m_i at i^{th} iteration or state) according to the Cauchy-like distribution, within the given bounds. Then the error $E(m_i)$ is calculated by Equation 5.9. If $E(m_i)$ is less than the $E(m_{i-1})$, the model m_i is accepted. For more details about VFSA algorithm, readers are referred to Sen and Stoffa, (2013).

6 Application of MHODE to gravity data

6.1 Synthetic Cases

In this section we will consider synthetic models simulating the geometry of a salt dome. In order to build a synthetic model, we consider first a salt dome, according to realistic geological settings (Gibson and Millegan, 1998). We will assume three different distributions of the density contrast, in order to simulate a realistic geological scenario. In all the examples we will perform a joint inversion (Equation 5.9) of the scaling functions for gravity, gravity gradient, 2nd order vertical derivative and 1st order vertical derivative of the horizontal gradient of gravity. The scaling function values are estimated along selected ridges, which we will describe below for each case.

As it regards τ_T, the theoretical expressions of g, $\partial g/\partial z$, $\partial^2 g/\partial z^2$ and $\partial^2 g/\partial z \partial x$ to insert in Equation 4.30 are calculated according to the Equations 3.11, 3.12, A.2 and A.3, respectively. A detailed description of each model will be given in the following sub-sections.

6.1.1 Case 1: Uniform density sources.

We first consider the model shown in Figure 6.1, this has a salt dome structure with a 2.3 g/cm^3 density inside the body and 2.5 g/cm^3 outside the body. This is the simplest geophysical scenario involving salt domes, referring to a homogeneous salt and a homogeneous background. The scaling functions of g, $\partial g/\partial z$, $\partial^2 g/\partial z^2$, $\partial^2 g/\partial z \partial x$ are estimated along the ridges from I to IX, shown in Figure 6.2 (a, b, c, d, respectively), at levels from 0 to 7.5 km, with a 0.4 km step. Ridges are determined by the zeros of the horizontal derivative for each of g, $\partial g/\partial z$, $\partial^2 g/\partial z^2$.

Assuming that the information of the top can be well retrieved by independent information, such as seismic, we performed a constrained inversion by fixing exactly the top of the body for depths from 1 to 1.5 km. We used wide bounds for searching the remaining vertices: $3 \leq x_q \leq 27$ km and $1.5 \leq z_q \leq 8$ km.

We started inverting for a few vertices, say 4, in order to make trials by changing initial temperature and number of iterations in VFSA. Once we got an optimal fitting between the observed and calculated values of the scaling function (Figure 6.3a), we incremented the number of vertices and inverted again using now 8 vertices (Figure 6.3b). The bounds are changed accordingly to the first estimate: we narrow the ranges of each vertex midway the coordinates of the nearest vertices, so honoring the information contained in the first model. We note that the misfit error of scaling function reduces passing from 4 to 8 vertices. So, continued with 12 vertices (Figure 6.3c) and then with 18 vertices, involving 36 unknowns (Figure 6.3c). This strategy proved that by increasing the number of vertices, the misfit error of scaling function reduces. A final good fitting is so obtained for all the scaling functions, as shown in Figure (Figure 6.4).

After having retrieved the geometry of the model, we passed to model the gravity field corresponding to the derived model. To do this, we needed however to estimate the value of the density contrast. This task may be easily performed by:

a) computing the gravity anomaly with a unit-density;
b) forming a scatter plot between this anomaly and the observed data;
c) computing a least-squares first-order polynomial regression analysis.

The slopes (Figure 6.5) yields: $\Delta\rho$ -0.201 g/cm^3, no matter the type of field involved (g, $\partial g/\partial z$, $\partial^2 g/\partial z^2$, $\partial^2 g/\partial z \partial x$), which is an accurate estimate of the assumed density contrast. Using this estimate for the density contrast and the sources geometry, we can compute the fields, which fit well the observed data (Figure 6.6).

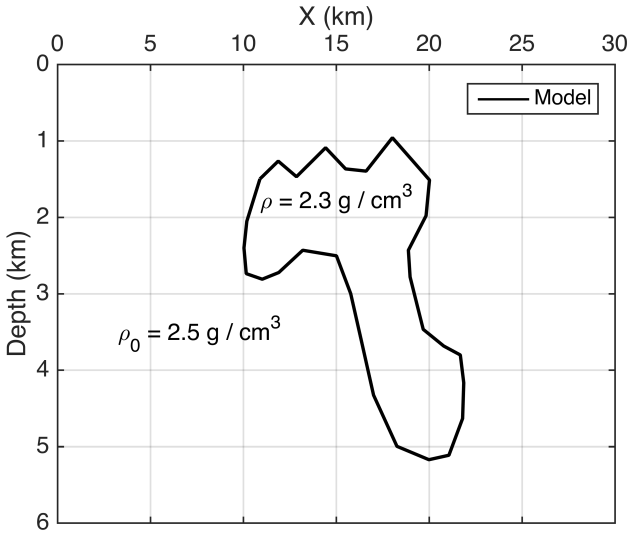

Figure 6.1 Assumed Source model, with density 2.3 g/cm3 inside the body and 2.5 g/cm3 outside the body.

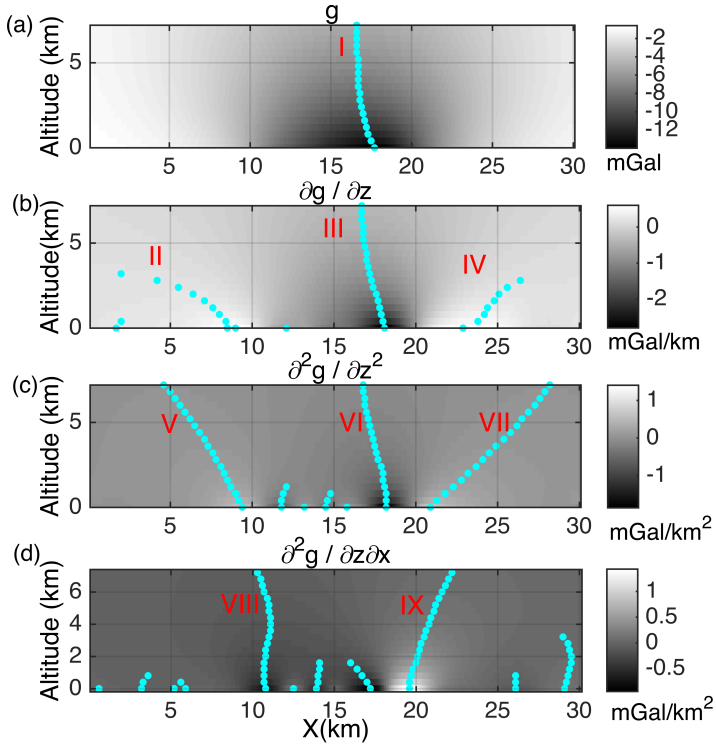

Figure 6.2 Fields due to the source model in Figure 6.1and calculated ridges (cyan dots) in a x-z section, for altitudes from 0 to 7.5 km. (a) ridges of g; (b) ridges of ∂g/∂z; (c) ridges of ∂²g/∂z²; (d) ridges of ∂²g/∂x∂z.

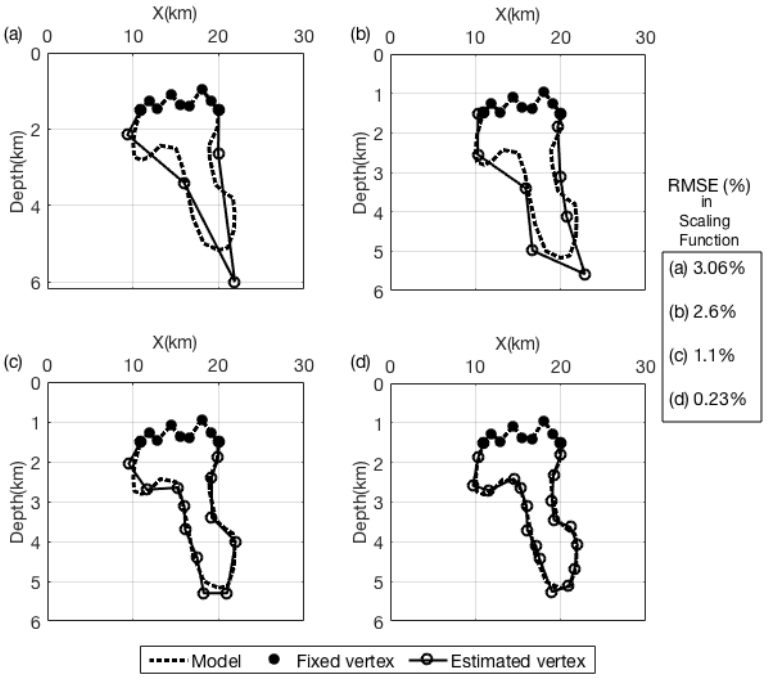

Figure 6.3 Comaprison between the true synthetic sources model (dotted line) and our estimated sources model (circles and solid line). Black solid circles show the vertices of the top-salt assumed as constraints, the other circles stand for the vertices estimated by inversion. Scaling functions are inverted assuming a model with, (a) four vertices (scaling function misfit error: 3.06%); (b) eight vertices (scaling function misfit error: 2.6%); (c) twelve vertices (scaling function misfit error: 1.1%); (d) eighteen vertices (scaling function misfit error:0.23%).

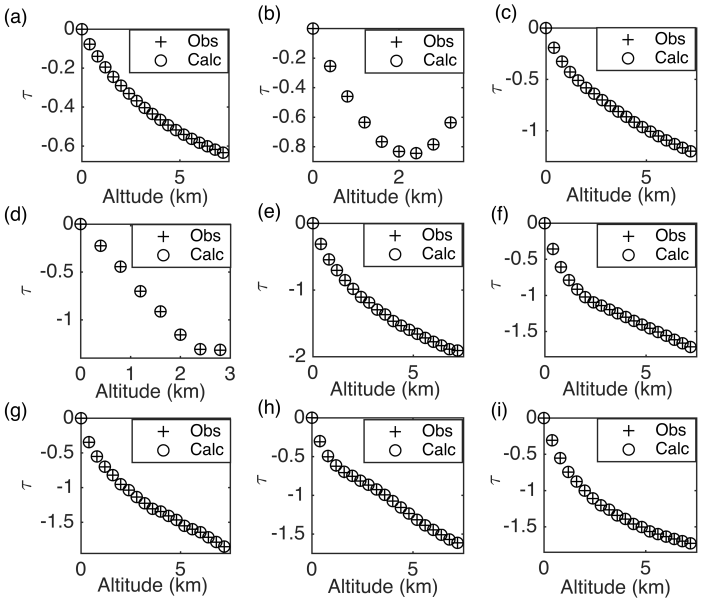

Figure 6.4 Observed and calculated scaling functions. (a) scaling function for g along ridge I (see Figure 6.2a); (b, c, d) scaling functions for ∂g/∂z along ridges II, III, IV (see Figure 6.2b); (e, f, g) scaling functions for ∂²g/∂z² along ridges V, VI, VII (see Figure 6.2c); (h, i) scaling functions for ∂²g/∂x∂z along the ridges VIII, IX (see Figure 6.2d).

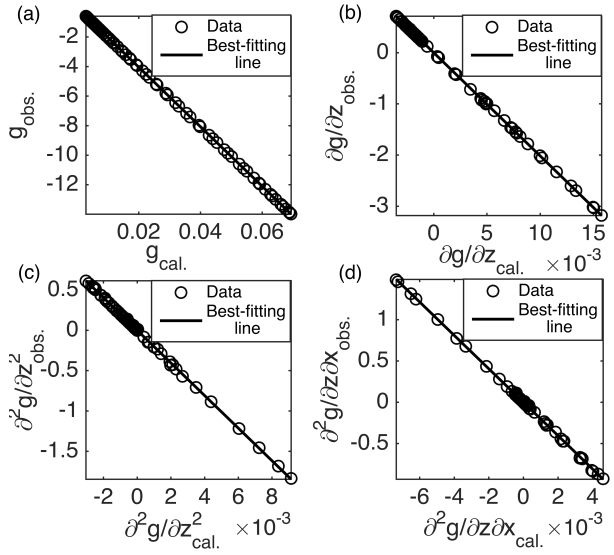

Figure 6.5 Scatter plot between calculated fields at unit-density and observed fields. By a first-degree polynomial fit we recover an estimation of the density contrast equal to – 0.21 g/cm3 for g, ∂g/∂z, ∂²g/∂z² and ∂²g/∂x∂z.

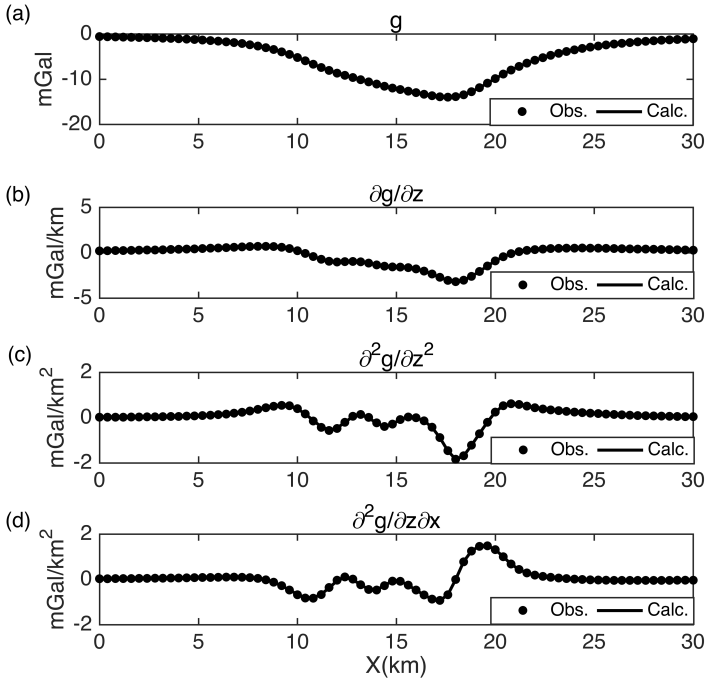

Figure 6.6 Observed and calculated anomalies for the salt dome in Figure 6.1. We assumed the model estimated in Figure 6.3d and the -0.21 g/cm^3 density contrast estimated in Figure 6.5. (a) g; (b) ∂g/∂z; (c) ∂²g/∂z²; (d) ∂²g/∂x∂z.

6.1.2 Case 2: Inhomogeneous sources with negative density contrast.

In this case we consider a more complex geological/geophysical situation for the salt dome, corresponding to a homogeneous salt density within the body and to a varying density out of the body, as caused by the presence of different sedimentary layers involving different densities (Reynold, 1997). This more complex scenario corresponds to subdividing the salt dome in three different parts with three different density contrasts: $\Delta\rho_1$ =-0.22 g/cm^3, $\Delta\rho_2$ =-0.18 g/cm^3 and $\Delta\rho_3$ =-0.30 g/cm^3, as shown in Figure 6.7. Following the same steps described in section 6.1.1, the gravity anomaly and its derivatives are calculated in *x*-*z* plane at altitudes from 0 to 7.5 km and further ridges are calculated for these fields (Figure 6.8). The scaling function is estimated for each ridge (numbered from I to IX) of the respective fields g, $\partial g/\partial z$, $\partial^2 g/\partial z^2$, $\partial^2 g/\partial z \partial x$.

Assuming again that the information of the top can be well retrieved by external information, such as seismic, we performed a constrained inversion by fixing exactly the top of the body for depths from 1 to 1.5 km. We used again wide bounds for searching the remaining vertices: $3 \leq x_q \leq 27$ km and $1.5 \leq z_q \leq 8$. This case shows the power of our method in a rather complex case, yielding a good reconstruction of the salt dome geometry without assuming any information about the density. In fact, as the scaling function does not depend on the density, we expect that our estimates should not be affected by a density contrast changing within the body. After running the algorithm for 1000 iterations, taking 2 minutes with a processor of 2x2.26 GHz Quad-Core Intel Xeon in a Mac Pro computer, we obtain in fact a source model (Figure 6.9) yielding a very good reconstruction of the salt dome model. The model produces scaling functions for g, $\partial g/\partial z$, $\partial^2 g/\partial z^2$, $\partial^2 g/\partial z \partial x$, which has a very good fitting vs. the observed scaling functions (Figure 6.10). As before, we have now to compute the salt density contrast allowing the reproduction of the observed anomalies g, $\partial g/\partial z$,$\partial^2 g/\partial z^2$ and $\partial^2 g/\partial z \partial x$. This time, however, we have a density contrast varying vs. depth, so that we should only account for a sort of average density contrast. After computing scatter plots among the anomalies generated with a unit-density and the observed data and computing a least-squares first-order polynomial regression analysis (Figure 6.11), we get a -0.22 g/cm^3 density contrast for all the fields (g, $\partial g/\partial z$, $\partial^2 g/\partial z^2$ and $\partial^2 g/\partial z \partial x$), which allows us

to fit fairly well the gravity anomaly and its derivatives (Figure 6.12). The calculated density is close to the weighted average density contrast (-0.226 g/cm^3) of the assumed model.

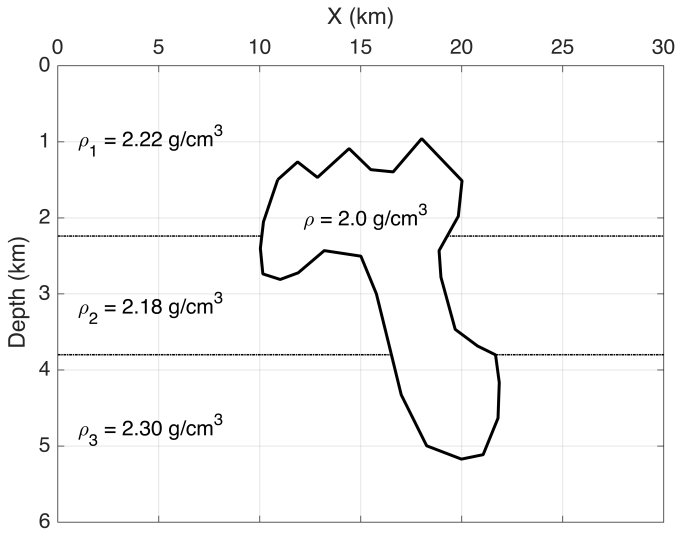

Figure 6.7 Assumed source model, characterized by having three different density contrasts: $\Delta\rho_1$ = -0.22 g/cm3, $\Delta\rho_2$ = - 0.18 g/cm3 and $\Delta\rho_3$ = -0.30 g/cm3.

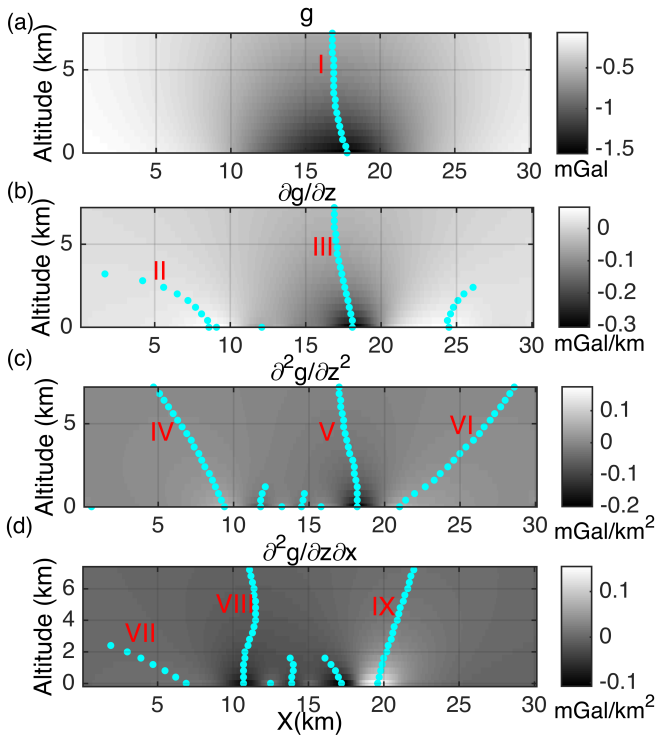

Figure 6.8 Fields due to the source model in Figure 6.7 and calculated ridges (cyan dots) in a x-z section, for altitudes from 0 to 7.5 km. (a) ridges of g; (b) ridges of ∂g/∂z; (c) ridges of ∂²g/∂z²; (d) ridges of ∂²g/∂x∂z.

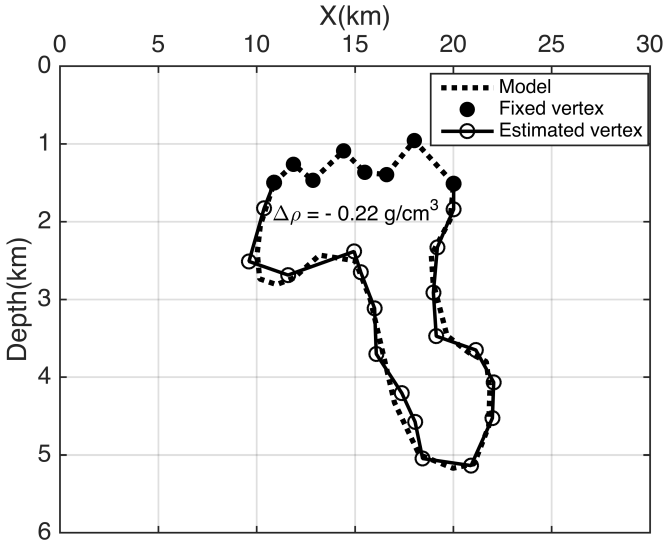

Figure 6.9 Comparison between the true synthetic source model (dotted line) and our estimated source model (circles and solid line). Black solid circles show the vertices of the top-salt assumed as constraints, black circles indicates the vertices estimated by inversion.

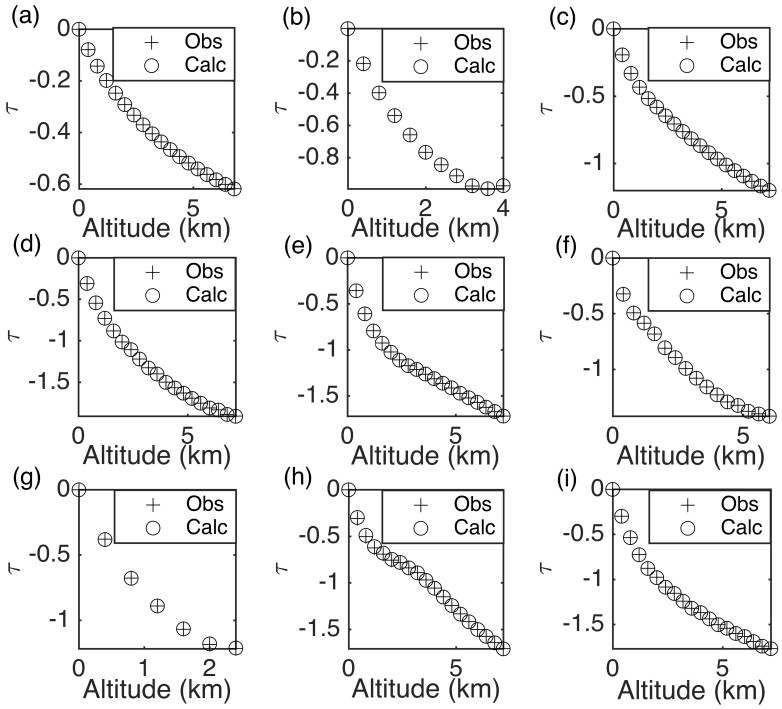

Figure 6.10 Observed and calculated scaling functions. (a) scaling function for g along ridge I (see Figure 6.8a); (b, c) scaling functions for ∂g/∂z along ridges II, III (see Figure 6.8b); (d,e, f) scaling functions for ∂²g/∂z² along ridges IV, V, VI (see Figure 6.8c); (g, h, i) scaling functions for ∂²g/∂x∂z along the ridges VII, VIII, IX (see Figure 6.8d).

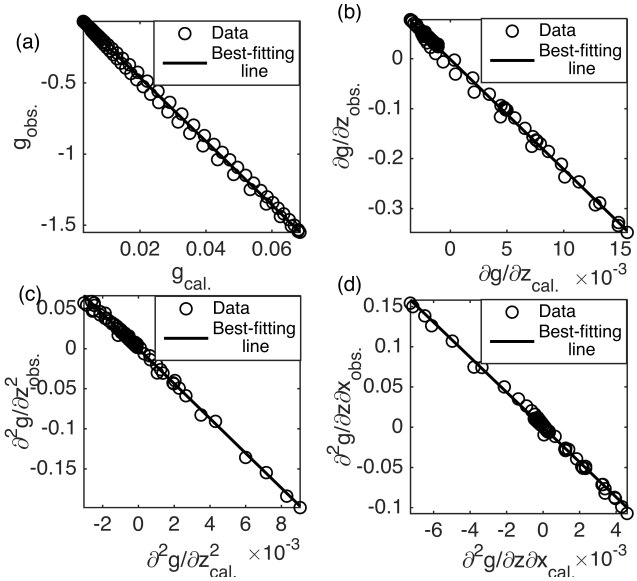

Figure 6.11 Scatter plots between calculated fields at unit-density and observed fields. By a first-degree polynomial fit we recover an estimation of the density contrast equal to: -0.22 g/cm3 for (a) g; (b) ∂g/∂z; ∂²g/∂z²; and (d) ∂²g/∂x∂z.

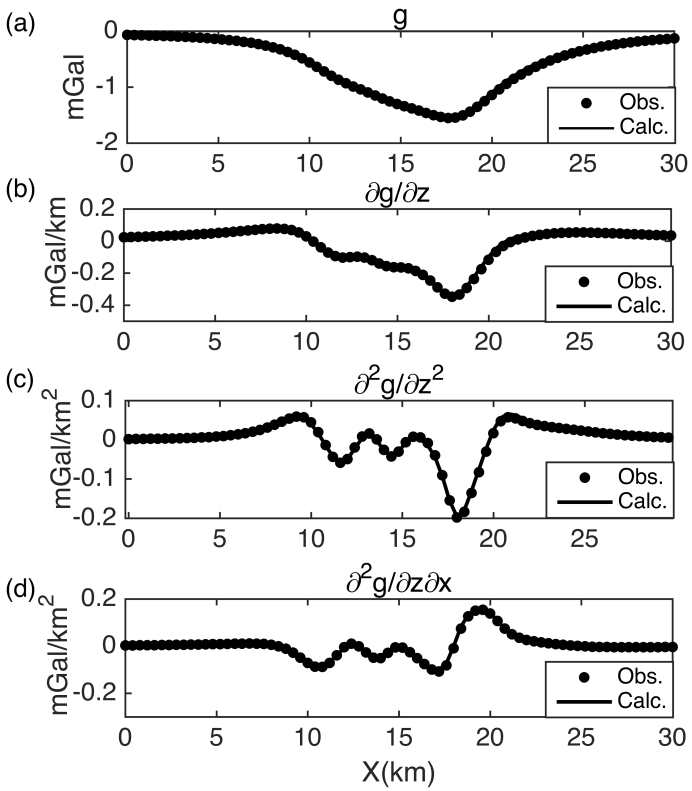

Figure 6.12 Observed and calculated anomalies for the salt dome in Figure 6.7. We assumed the model estimated in Figure 6.9 and the density contrasts estimated in Figure 6.11. (a) g; (b) $\partial g/\partial z$; (c) $\partial^2 g/\partial z^2$; (d) $\partial^2 g/\partial x \partial z$.

6.1.3 Case 3: Inhomogeneous sources with positive and negative density contrasts.

In this section we simulated the most complex case for a salt dome anomaly: we assume in fact that the top part of the body has a positive density contrast while the rest of the body has various values of negative density contrasts. This corresponds to subdividing the source in 4 parts each one with its density contrast, as shown in Figure 6.13, where $\Delta\rho_1$ = 0.10 g/cm^3, $\Delta\rho_2$ = -0.10 g/cm^3, $\Delta\rho_3$ = -0.13 g/cm^3 and $\Delta\rho_4$= -0.17 g/cm^3. This situation is common for shallow salt domes: their top part is, as a matter of fact, denser than the background sedimentary layer, while the sign of the density contrast changes at greater depths (Gibson and Millegan, 1998; Krahenbuhl and Li, 2006).

Following the same steps described in section 6.1.1, the gravity anomaly and its derivatives are calculated in *x*-*z* plane at altitudes from 0 to 6 km with a 0.3 km step and ridges are calculated for these fields (Figure 6.13). The scaling function is estimated for

each ridge (numbered from I to VIII) of the respective fields g, $\partial g/\partial z$, $\partial^2 g/\partial z^2$, $\partial^2 g/\partial z \partial x$.

We started the inversion similarly as mentioned above in sections 6.1.1 and 6.1.2, letting VFSA to run for 1000 iterations. This time, however, we have a partial annihilation effect (Parker, 1977) for the gravity field, meaning that the field from the top part of the salt dome tends to cancel partially the remaining salt dome effect, caused instead by a negative density contrast. This is obviously due to the linear properties of the potential fields, because these two kinds of contributions to the field sum up algebraically. This is an inherent ambiguity problem in inversion of potential fields and can only be fixed by using external information (Parker, 1977). So, this time, we must work under the more restrictive hypothesis that we can assume both a geometrical and a density model of the top part of the body, from a seismic velocity model. Consequently, we calculated the gravity anomaly for the top part of the body and subtracted it from the observed gravity anomaly. The inversion, once again, gives a good reconstruction of the source model (Figure 6.15) and such model produces scaling functions for g, $\partial g/\partial z$, $\partial^2 g/\partial z^2$, $\partial^2 g/\partial z \partial x$, which have a good fitting vs. the observed scaling functions (Figure 6.16). Figure 6.17 shows the scatter plots for g, $\partial g/\partial z$, $\partial^2 g/\partial z^2$ and $\partial^2 g/\partial z \partial x$ among the anomalies generated with a unit-density and the observed data, yielding, through a least-squares first-order polynomial regression analysis the following density contrasts: -0.13 g/cm^3 for g and $\partial g/\partial z$ and -0.12 g/cm^3 for $\partial^2 g/\partial z^2$ and $\partial^2 g/\partial z \partial x$. As in the previous case, they must be interpreted as equivalent density contrast, which are in fact close to the weighted average density contrast -0.1286 g/cm^3 of the assumed model for the middle and low part of the salt. Residual anomalies generated by the middle and low parts of the body (i.e., that having a negative density contrast) are shown in Figure 6.18.

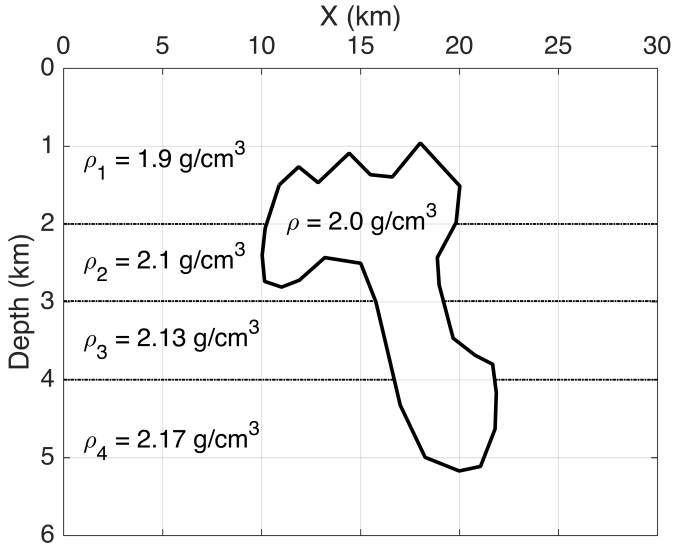

Figure 6.13 Assumed source model, which is now relative to four different density contrasts: $\Delta\rho_1$ = 0.1 g/cm3, $\Delta\rho_2$ = - 0.1 g/cm3 and $\Delta\rho_3$ = -0.13 g/cm3 and $\Delta\rho_4$= -0.17 g/cm3

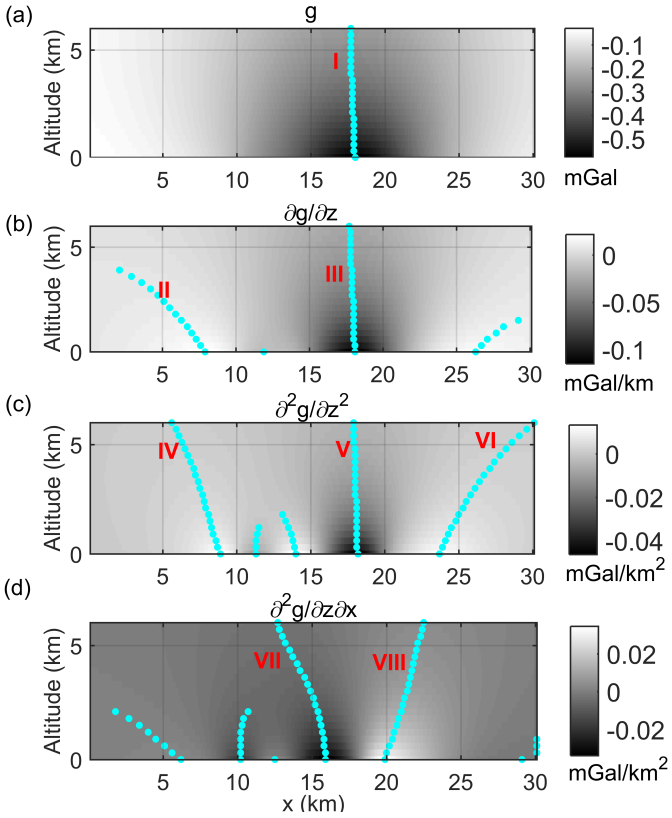

Figure 6.14 Fields due to the source model in Figure 6.13 and calculated ridges (cyan dots) in a x-z section, for altitudes from 0 to 6 km. (a) calculated ridge for g; (b) calculated ridges for ∂g/∂z; (c) calculated ridges for ∂²g/∂z²; (d) calculated ridges for ∂²g/∂x∂z.

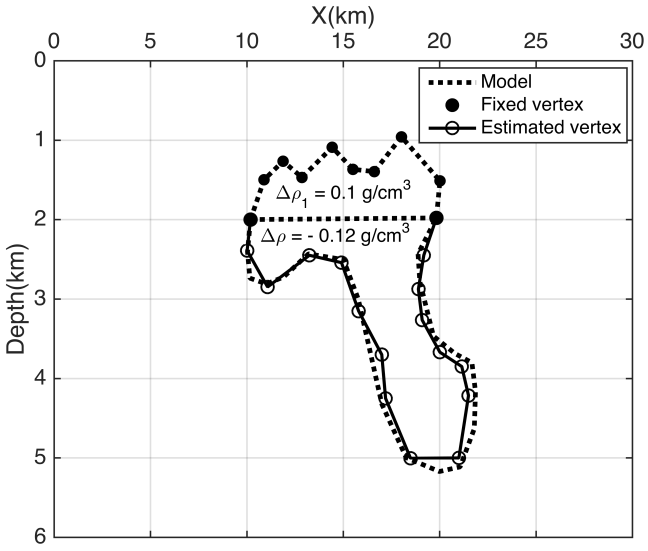

Figure 6.15 Comparison between the true synthetic source model (dotted line) and our estimated source model (circles and solid line). Black solid circles show the vertices of the top-salt assumed as constraints, black circles indicates the vertices estimated by inversion.

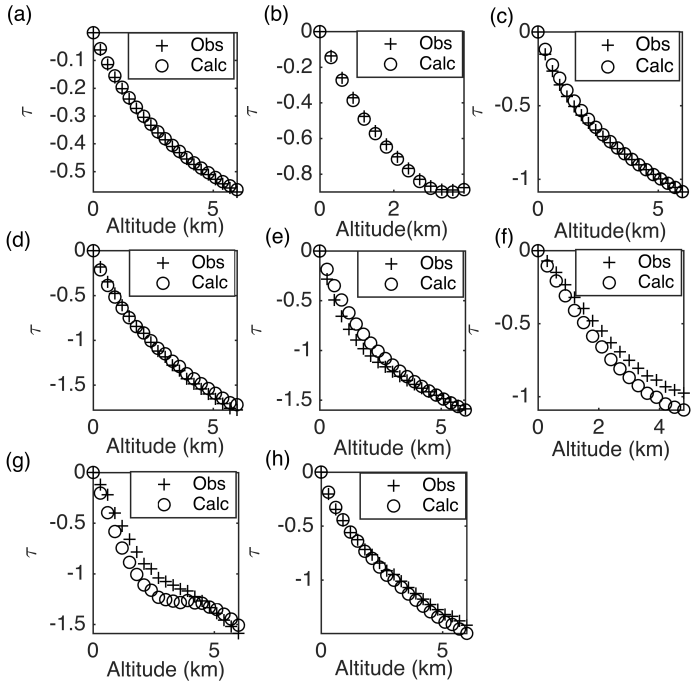

Figure 6.16 Observed and calculated scaling functions. (a) scaling function for g along ridge I (see Figure 6.14a); (b, c) scaling functions for ∂g/∂z along ridges II, III (see Figure 6.14b); (d, e, f) scaling functions for ∂²g/∂z² along ridges IV, V, VI (see Figure 6.14c); (g, h) scaling functions for ∂²g/∂x∂z along the ridges VII, VIII (see Figure 6.14d).

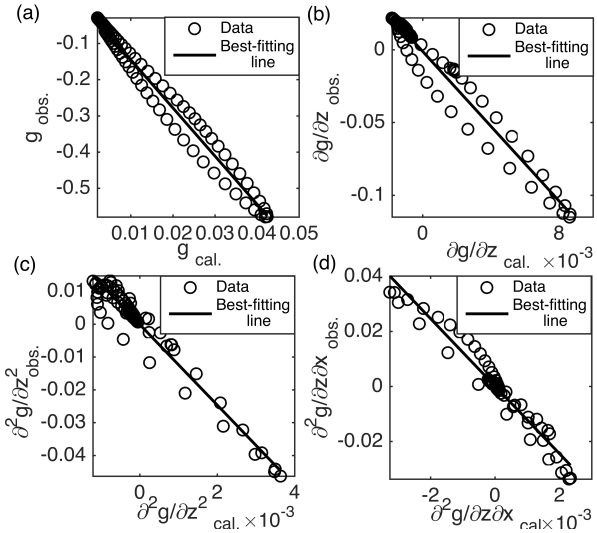

Figure 6.17 Scatter plots between calculated fields at unit-density and observed fields. By a first-degree polynomial fit we recover an estimation of the density contrast equal to: (a) -0.13 g/cm3 for g; (b) -0.13 g/cm3 for ∂g/∂z; (c) -0.12 g/cm3 for ∂²g/∂z²; (d) -0.12 g/cm3 for ∂²g/∂x∂z.

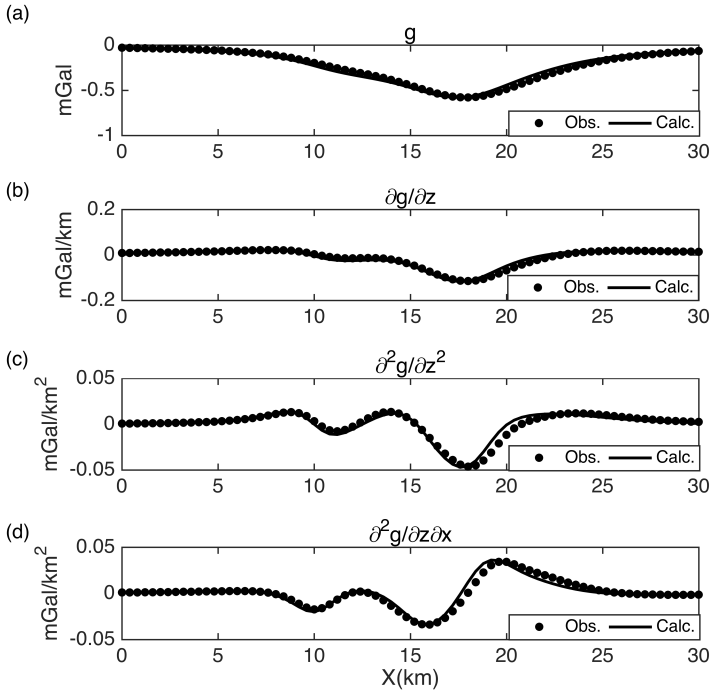

Figure 6.18 Observed and calculated anomalies for the salt dome in Figure 6.14. We assumed the model estimated in Figure 6.15 and the density contrasts estimated in Figure 6.17. (a) g; (b) ∂g/∂z; (c) ∂²g/∂z²; (d) ∂²g/∂x∂z.

6.2 Real data inversion

6.2.1 Mors salt dome, Denmark (waste disposal).

We study here the Bouguer anomaly over the Mors salt dome in Northern Jutland (Reynolds, 1997). Initial study of this anomaly was made for safe disposal of radioactive material (Sharma, 1986; Reynolds, 1997), but obviously the interest for salt structures is specially because it is a feasible environment for hydrocarbons. We digitized the anomaly data from the map in Figure (2.37) of Reynolds (1997).

In order to calculate the ridges of the given anomaly, we performed an upward continuation (Blakely, 1996) of the data and computed its first-order derivatives at altitudes from 0 to 3 km; then we computed the field ridges for g, $\partial g/\partial z$ and $\partial g/\partial x$ (Figure 6.19) along a vertical section, along the same profile considered by several authors (see Reynolds, Figure 2.38). We limited our computations to the first-order derivatives only, due to our coarse digitization of the published data map, which did not allow us good results at higher orders. So, we calculated the scaling function along the ridges from I to IV, as shown in Figure 6.19 for g, $\partial g/\partial z$ and $\partial g/\partial x$. The noise level is however relatively high for the field derivatives at the lowest altitudes, as shown by the great number of maxima at these altitudes; however, for multiscale methods, we can well regularize the problem by simply excluding such data from the analysis (e.g., Florio and Fedi, 2014: Figure 6). Therefore, we choose the investigation altitudes as: 0 to 3 km for g and 0.8 to 3 km for $\partial g/\partial x$ and $\partial g/\partial z$. Afterwards, we adopted the same procedure as for the synthetic cases, using the VFSA algorithm for inverting the scaling functions of the above-indicated fields. Once again, we assumed to have good information about the top of the source and fixed a few vertices at the salt top during inversion, as constraints. If we consider that the profile length is 16.1 km, we used wide bounds for searching the remaining vertices: $2 \leq x_q \leq 14.5$ km and $1.5 \leq z_q \leq 8$ km. After 1000 iterations we reached an optimal solution (Figure 6.20) that fits rather well the observed scaling functions for g, $\partial g/\partial z$ and $\partial g/\partial x$ (Figure 6.21). You may also see in Figure 6.20 that the estimated source model resembles the gravity-based model built by other authors (Kreitz, 1982; LaFehr, 1982; Sharma, 1986; Reynolds, 1997); differently from us, however, these authors assumed a priori information for the density contrast. This source model was then

used to calculate the field anomalies g, $\partial g/\partial z$ and $\partial g/\partial x$ by assuming a unit-density. We used them to build scatter plots and to compute the average density contrasts of the salt dome by the slope of the 1st order regression line (Figure 6.22). The retrieved density values were: -0.17 g/cm^3 for g, -0.16 g/cm^3 for $\partial g/\partial x$ and -0.17 g/cm^3 for $\partial g/\partial z$. These values were finally utilized to compare the anomalies computed from our estimated model to the g, $\partial g/\partial z$ and $\partial g/\partial x$ anomalies (Figure 6.23).

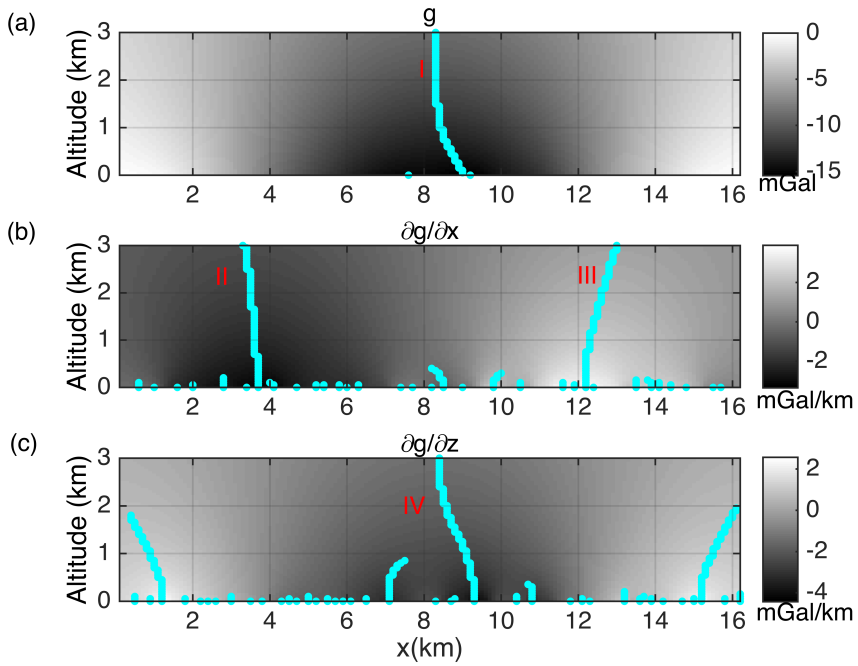

Figure 6.19 Fields and calculated ridges (cyan dots) in a x-z section, for altitudes from 0 to 4 km (a) calculated ridges for g; (b) calculated ridges for ∂g/∂x; (c) calculated ridges for ∂g/∂z.

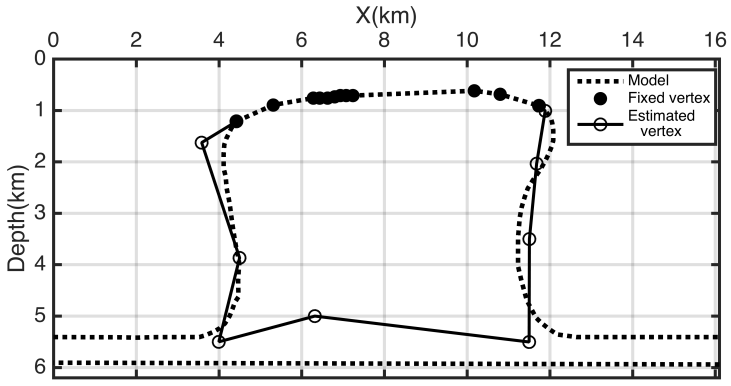

Figure 6.20 Estimated source model (solid line, black circles) with MHODE method and model (dotted line) as interpreted by Sharma (1986) and Reynolds (1997). Solid black dots show the fixed vertices of the body during inversion.

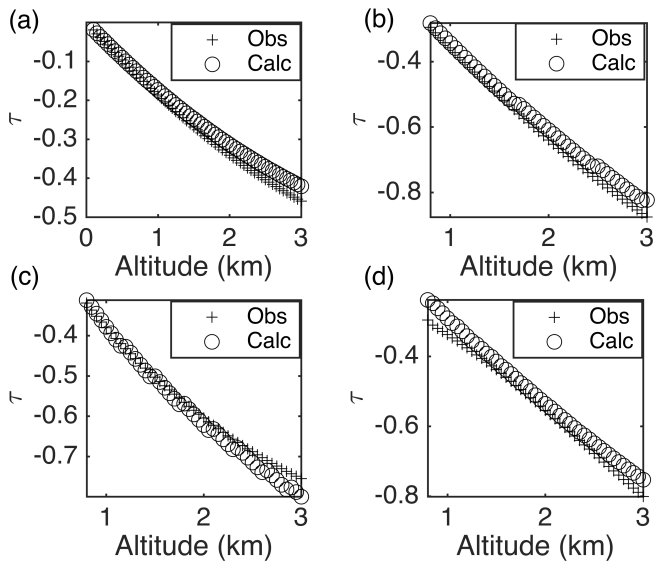

Figure 6.21 Observed and calculated scaling functions. (a) scaling function for g along ridge I (see Figure 6.19a); (b, c) scaling functions for ∂g/∂x along ridges II, III (see Figure 6.19b); (d) scaling functions for ∂g/∂z along ridges IV (see Figure 6.19c).

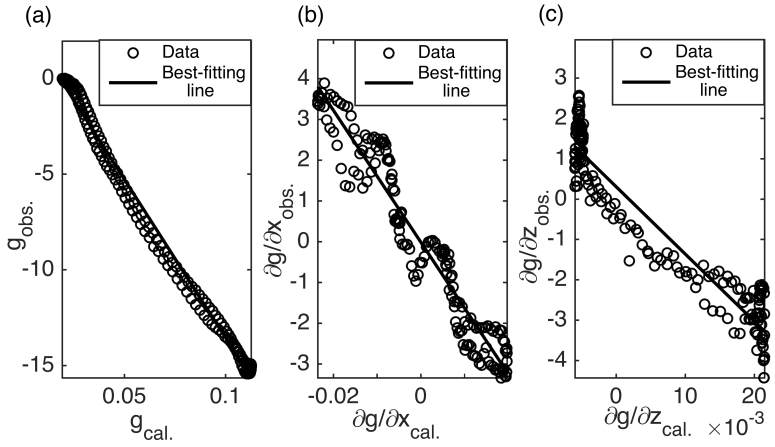

Figure 6.22 Scatter plots between calculated fields at unit-density and observed fields. By a first-degree polynomial fit we recover an estimation of the density contrast equal to: (a) -0.17 g/cm3 for g; (b) -0.16 g/cm3 for ∂g/∂x; (c) -0.17 g/cm3 for ∂g/∂z.

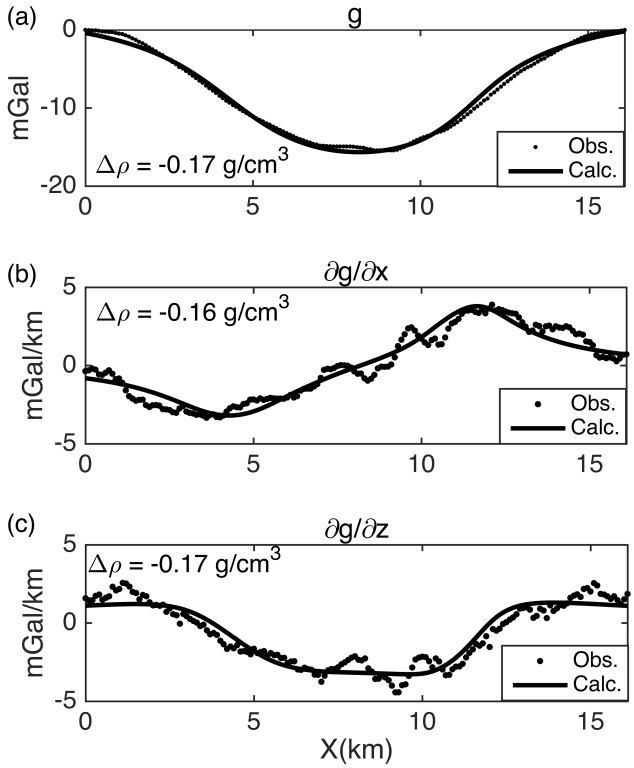

Figure 6.23 Observed and calculated anomalies for the Mors salt dome in Figure 6.19. We assumed the source geometry estimated in Figure 6.20 (black circles) and the density contrasts estimated in Figure 6.22. (a) g; (b) ∂g/∂x; (c) ∂g/∂z.

6.2.2 Godavri basin (Andhra Pradesh, India)

As a second real-data case, we interpret the gravity profile of Godavari basin, Andhra Pradesh, India. The data, shown in Figure 6.28(a), were digitized from Rao (1990). The profile is over the lower Godavari valley, located approximately at 17° N and 81° E, with strike direction NW-SE. Rao (1990) considered a simple trapezoidal model and inverted using Marquardt algorithm assuming -0.4 g/cm^3 density contrast.

We first calculated the horizontal and vertical derivative of the data and thereafter continued them and the gravity data themselves up to 2.5 km, in order to calculate the respective ridges, indicated in Figure 6.24 with numbers from I to IV. Even in this real case, we limited our analysis to the 1st order field derivatives and selected the altitudes for the field derivatives as those greater than 0.6 km. This because the signal-to-noise ratio

was too low at altitudes lower than 0.6 km, as demonstrated by the elevated number of maxima occurring in that scale range (Florio and Fedi, 2014). Inversion by VFSA algorithm was then performed on the scaling function calculated along the ridges of g, $\partial g/\partial x$ and $\partial g/\partial z$, yielding the estimated source model shown in Figure 6.25. Note that it is close to the trapezoidal model used by Rao (1990), but that, in our case, it has been estimated without any a priori information about the density contrast and depth constraints.

The scaling functions, computed for g, $\partial g/\partial x$ and $\partial g/\partial z$ after the estimated source model, fit well the scaling functions of the measured data, as shown in Figure 6.25. We then estimated the average density contrast for the source after computing the scatter plots for g, $\partial g/\partial x$ and $\partial g/\partial z$ (Figure 6.27), obtaining -0.43 g/cm^3 for g, -0.41 g/cm^3 for $\partial g/\partial x$ and -0.44 g/cm^3 for $\partial g/\partial z$. The estimated contrasts are slightly higher than that used by Rao (1990): -0.4 g/cm^3. Finally, we used the calculated density contrasts to compute the field anomalies, which fit fairly well the original data (Figure 6.28).

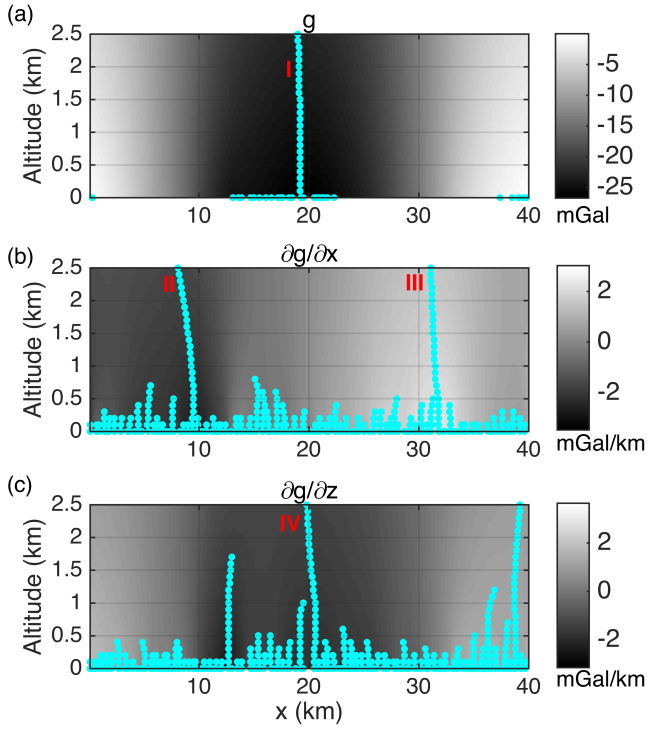

Figure 6.24 Fields and calculated ridges (cyan dots) in a x-z section, for altitudes from 0 to 2.5 km; (a) calculated ridge for g; (b) calculated ridges for ∂g/∂x; (c) calculated ridges for ∂g/∂z.

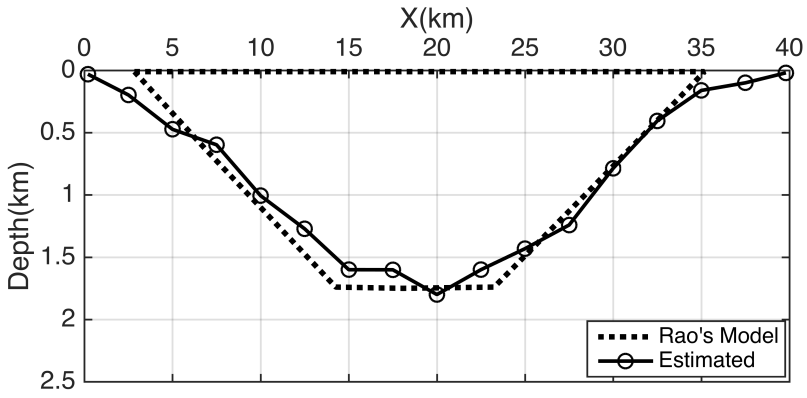

Figure 6.25 Estimated source model (solid line and circles) with MHODE method and model (dotted line) as interpreted by Rao (1990).

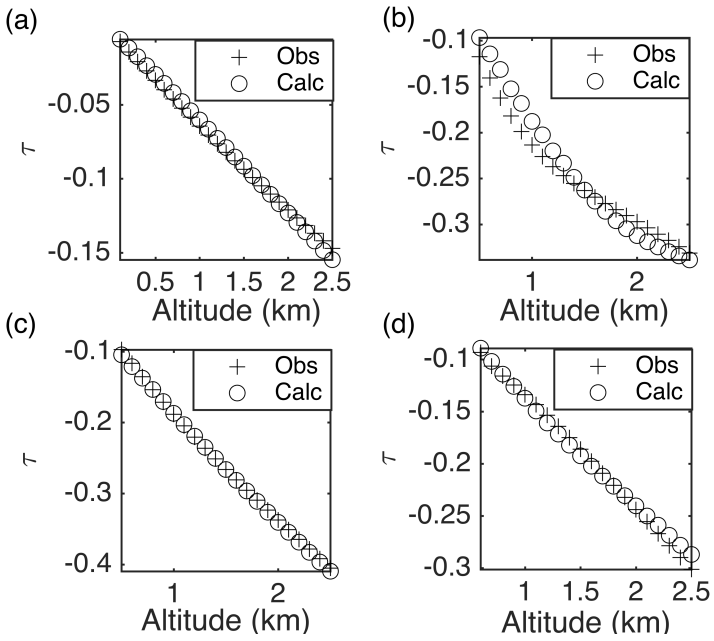

Figure 6.26 Observed and calculated scaling functions. (a) scaling function for g along ridge I (see Figure 6.24a); (b, c) scaling functions for ∂g/∂x along ridges II, III (see Figure 6.24b); (d) scaling functions for ∂g/∂z along ridges IV (see Figure 6.24c).

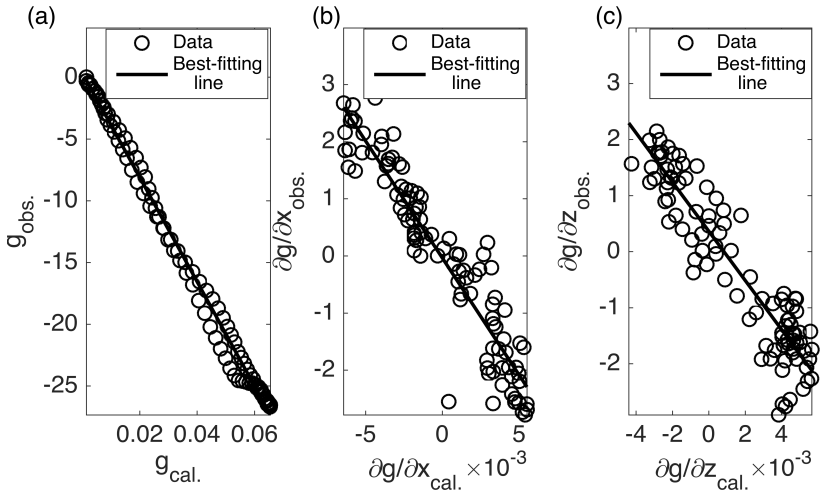

Figure 6.27 Scatter plots among calculated fields at unit-density and observed fields. By a first-degree polynomial fit we recover an estimation of the density contrast equal to: (a) -0.43 g/cm3 for g; (b) -0.41 g/cm3 for ∂g/∂x; (c) -0.44 g/cm3 for ∂g/∂z.

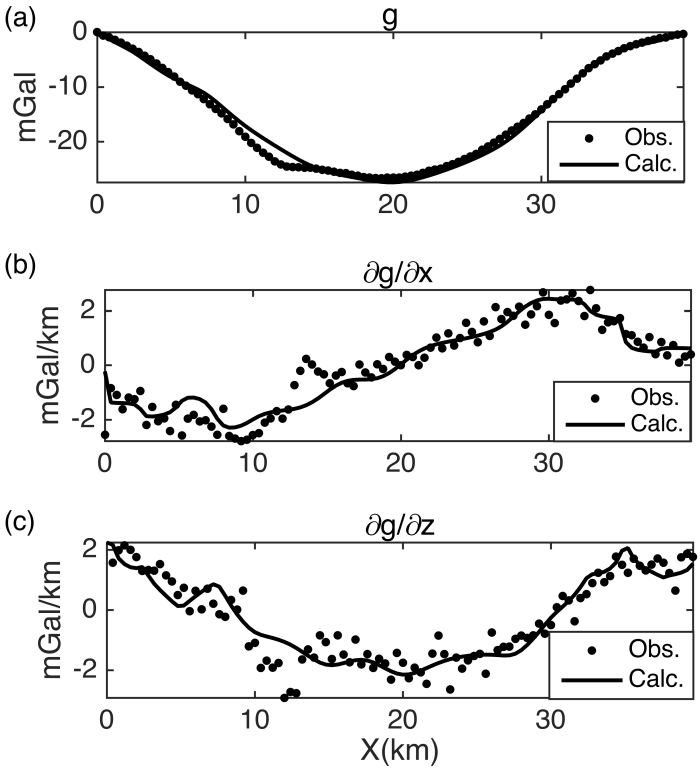

Figure 6.28 Observed and calculated anomalies for the Godavari Basin, as estimated in Figure 6.24. We assumed the source geometry estimated in Figure 6.25 (black circles) and the density contrasts estimated in Figure 6.27. (a) g; (b) ∂g/∂x; (c) ∂g/∂z.

7 Conclusions and Perspective

In this thesis, I have presented an automatic multi-scale inversion method to interpret potential fields generated by complex sources. We assumed a multi-source body in the form of the Talwani's formula, which allows the inversion for the source positions of a number of vertices specified by the interpreter.

The most significant feature of the method is that the inversion is not applied directly to the field anomaly data but to the scaling function values. This has three-fold advantages:

a) the scaling function is independent of density and other physical constants and this property makes the inversion less ambiguous than the field inversion;
b) the inversion is performed according to the MHODE method involving the scaling function evaluated along the field ridges, that is a set of few points at different scales, where the horizontal derivatives of the field (or of its derivatives) are zero. This means that only few data are involved in the inversion, reducing the numerical complexity of the problem;
c) due to the above property and to the inherent stability of the multiscale methods, we may use ridges of the field derivatives, either vertical or horizontal.

However, the method needs the forward problem to be formulated in terms of the scaling function, which involves new mathematical and numerical formulations for the problem. This was made in this thesis for the 2D gravity problem in terms of Talwani's formula and formulas are given also for the derivatives of the gravity field up to the second order. Other formulations may be however investigated as well its extension to the case of 3D sources.

In any case, the non-linearity of the scaling function equations adds complexity to the solution retrieval. In this thesis, we address this issue efficiently by using the VFSA

algorithm, which does not necessarily require a good starting model. The only constraints needed are reasonable bounds for the search of the solution.

We described applications of the method to both synthetic and real-data cases. In order to reduce the ambiguity of the problem we studied the special case in which the top of the source is partially fixed by external information, as in the case of top of salt domes, which is often very well defined by seismic data. The solution provided by this method is very accurate in defining those parts of the domes (flanks and bottom), which are normally poorly defined by seismic data.

Moreover, using three different scenarios of density contrast distributions we showed that the inversion of a quantity independent on density (the scaling function) is really advantageous for managing also complex cases, included that in which the density contrast assumes opposite signs vs. depth.

The application to the real case of the Mors salt dome and of the Godavari basin, India, confirmed the validity of the method, yielding solutions in good agreement with models constructed by other researchers. The interest of our method is that our models are obtained without a priori density information and with constrains regarding only the top to the source.

Future research will regard the statistical analysis of the inversion results and formulation of the current method for the magnetic case. Other development will regard the extension of the method for interpreting data due to 3D sources.

8 References

Abbas, M.A., M. Fedi, and G. Florio, 2014, Improving the local wavenumber method by automatic DEXP transformation: Journal of Applied Geophysics, 111, 250– 255, doi: 10.1016/j.jappgeo.2014.10.004.

Abbas, M.A., and M. Fedi, 2014, Automatic DEXP imaging of potential fields independent of the structural index: Geophysical Journal International, 199, 1625-1632, doi: 10.1093/gji/ggu354.

Baniamerian, J., M. Fedi, and B. Oskooi, 2016, Research note: Compact depth from extreme points: A tool for fast potential field imaging: Geophysical Prospecting, 64, no. 5, 1386-1398, doi: 10.1111/1365-2478.12365.

Blakely, R., 1996, Potential theory in gravity and magnetic applications: Cambridge University Press.

Camacho, A., F. Montesinos, and R. Vieira, 2000, Gravity inversion by means of growing bodies: Geophysics, 65, no. 1, 95–101, doi: 10.1190/1.1444729.

Canny, J., 1986, A computational approach to edge detection: IEEE Transactions on Pattern Analysis and Machine Intelligence, 8, 679–698.

Cella, F., and M. Fedi, 2012, Inversion of potential field data using the structural index as weighting function rate decay: Geophysical Prospecting, 60, 313–336.

Chauhan, M. S., and M. Fedi, 2015, Multiple source estimation from potential field data by the MHODE method: 85th Annual International Meeting, SEG, Expanded Abstracts, 1510-1514, doi: 10.1190/segam2015-5877038.1.

Dimri, V., 1992, Deconvolution and Inverse Theory- Application to geophysical problems: Elsevier.

Fedi, M., and A. Rapolla, 1999, 3-D Inversion of gravity and magnetic data with depth resolution: Geophysics, 64, no. 2, 452-460, doi: 10.1190/1.1444550.

Fedi, M., 2007, DEXP: A fast method to determine the depth and the structural index of potential fields sources: Geophysics, 72, no. 1, I1–I11, doi: 10.1190/1.2399452.

Fedi, M., G. Florio, and T. Quarta, 2009, Multiridge analysis of potential fields: Geometric method and reduced Euler deconvolution: Geophysics, 74(4), L53–L65, doi: 10.1190/1.3142722.

Fedi, M., F. Cella, T. Quarta, and A. Villani, 2010, 2D continuous wavelet transform of potential fields due to extended source distributions: Applied and Computational Harmonic Analysis, 28, no. 3, 320–337, doi: 10.1016/j.acha.2010.03.002.

Fedi, M., and L. Cascone, 2011, Composite continuous wavelet transform of potential fields with different choices of analyzing wavelets: Journal of Geophysical Research, 116, B7, doi:10.1029/2010JB007882.

Fedi, M., G. Florio, L. Cascone, 2012. Multiscale analysis of potential fields by a ridge consistency criterion: the reconstruction of the Bishop basement: Geophysical Journal International, 188, 103–114, doi: 10.1111/j.1365-246X.2011.05259.x.

Fedi, M., and M. Pilkington, 2012, Understanding imaging methods for potential field data: Geophysics, 77(1), G13–G24, doi: 10.1190/geo2011-0078.1.

Fedi, M., and G. Florio, 2013, Determination of the maximum-depth to potential field sources by a maximum structural index method: Journal of Applied Geophysics, 88, 154–160, doi: 10.1016/j.jappgeo.2012.10.009.

Fedi, M., G. Florio, and V. Paoletti, 2015, MHODE: a local-homogeneity theory for improved source- parameter estimation of potential fields: Geophysical Journal International, 202, no. 2, 887-900, doi: 10.1093/gji/ggv185.

Fedi, M., 2016, Scaling laws in geophysics: Application to potential fields of methods based on the laws of self-similarity and homogeneity, in V. P. Dimri, Fractal Solutions for Understanding Complex Systems in Earth Sciences, Springer International, Cham, Switzerland, 1–18.

Florio, G., and M. Fedi, 2014, Multiridge Euler deconvolution: Geophysical Prospecting, 62, no. 2, 333– 351. http://dx.doi.org/10.1111/1365-2478.12078.

Gerovska, D., P. Stavrev, and M.J. Arauzo-Bravo, 2005. Finite difference Euler deconvolution algorithm applied to the interpretation of magnetic data from Northern Bulgaria: Pure and Applied Geophysics, 162, 591– 608.

Gibert, D., A. Galdéano, 1985, A computer program to perform transformations of gravimetric and aeromagnetic surveys: Computer and Geoscience, 11, 553–588.

Gibson, R. I., and P. S. Millegan, 1998, Geologic applications of gravity and magnetics: Case histories: SEG and AAPG.

Hinze, W. J., R. R. B. von Frese, and A. H. Saad, 2013, Gravity and magnetic exploration: Cambridge University Press.

Ingber, L., 1989, Very fast simulated reannealing, Mathematical and Computer Modeling, 12, no. 8. 967–993.

Ingber, L., 1993, Simulated annealing: Practice versus theory: Mathematical and Computer Modeling, 18, no 11, 29–57.

Keating, P., and M. Pilkington, 2004. Euler deconvolution of the analytic signal and its application to magnetic interpretation, Geophysical Prospecting, 52, 165–182.

Kearey P., M. Brooks, and I. Hill, 2002, An Introduction to Geophysical Exploration: Blackwell Publishing, Oxford.

Kellogg, O.D., 1928, Foundations of Potential Theory: Dover Publications Inc.

Kirkpatrick, S.C., D. Gelatt, and M. P. Vecchi, 1983, Optimization by simulated annealing: Science, 220, 671–680, doi: 10.1126/science.220.4598.671.

Krahenbuhl, R. A., and Y. Li, 2006, Inversion of gravity data using a binary formulation: Geophysical Journal International, 167, 543–556, doi: 10 .1111/gji.2006.167.issue-2.

Kreitz, E., 1982, Seismic evaluation of the Mors salt dome, in Results of Geological Investigations for High-Level Waste Disposal in the Mors Salt Dome, Proceedings of a Symposium, 18-19 Sept. 1981, Copenhagen, 1,74-98.

LaFehr, T.R., 1982, Evaluation of surface and borehole gravity measurements at the Mors salt dome, in Results of Geological Investigations for High-Level Waste Disposal in the Mors Salt Dome, Proceedings of a Symposium, 18-19 Sept. 1981, Copenhagen, 1, 196-232.

Li, Y. and D. W. Oldenburg, 1996, 3D inversion of magnetic data: Geophysics, 61, no. 2, 394–408, doi: 10.1190/1.1443968.

Li, Y., and D. W. Oldenburg, 1998, 3-D inversion of gravity data: Geophysics, 63, no. 1, 109–119, doi: 10.1190/1.1444302.

Mastellone, D., M. Fedi, S. Ialongo, and V. Paoletti, 2014, Volume Continuation of potential fields from the minimum-length solution: An optimal tool for continuation

through general surfaces: Journal of Applied Geophysics, 111, 346-355, doi: 10.1016/j.jappgeo.2014.10.020.

Menke, W., 1989. Geophysical Data Analysis: Discrete Inverse Theory: Academic Press, p. 289, (ISBN 01249092130).

Moreau, F., D. Gibert, M. Holschneider, and G. Saracco, 1997, Wavelet analysis of potential fields: Inverse Problems, 13, no. 1, 165–178, doi: 10.1088/0266-5611/13/1/013.

Nabighian, M. N., 1972, The analytic signal of two-dimensional magnetic bodies with polygonal cross-section: Its properties and use for automated anomaly interpretation: Geophysics, 37, 507–517.

Nagihara, S., and S. A. Hall, 2001, Three-dimensional gravity inversion using simulated annealing: Constraints on the diapiric roots of allochthonous salt structures: Geophysics, 66, no. 5, 1438–1449, doi: 10.1190/1.1487089.

Oppenheim, A.V., R.W. Schafer, 1975. Digital Signal Processing. Prentice-Hall, p. 608.

Paoletti V., P. C. Hansen, M. F. Hansen, and M. Fedi, 2014, A Computationally efficient tool for assessing the depth resolution in potential field inversion: Geophysics, 79, no. 4, A33-A38, doi: 10.1190/geo2014-0017.1.

Parker, R. L., 1977, Understanding inverse theory: Annual Review of Earth and Planetary Science, 5, 35–64, doi: 10.1146/annurev.ea.05.050177.000343.

Pedersen, L. B., 1989, Relations between horizontal and vertical gradients of potential fields: Geophysics, 54, 662-663, doi: 10.1190/1.1442694.

Pilkington, M., 1997, 3-D magnetic imaging using conjugate gradients: Geophysics, 62, 1132–1142, doi: 10.1190/1.1444214.

Rao, D. B., 1990, Analysis of gravity anomalies of sedimentary basins by an asymmetrical trapezoidal model with quadratic density function: Geophysics, 55, no. 2, 226-31, doi: 10.1190/1.1442830.

Ravat, D., 1994. Use of fractal dimension to determine the applicability of Euler's homogeneity equation for finding source locations of gravity and magnetic anomalies, in Proceedings of the Symposium on the Application of Geophysics to Engineering and Environmental problems, Boston, March 1994, Environmental and Engineering Geophysical Society, Englewood, CO, 41–53.

Ravat D., 1996, Analysis of the Euler method and its applicability in environmental investigations: Journal of Environmental and Engineering Geophysics, 1, 229–238.

Reid, A. B., J. M. Allsop, H. Granser, A. J. Millett, and I. W. Somerton, 1990, Magnetic interpretation in three dimensions using Euler deconvolution: Geophysics, 55, no. 1, 80– 91, doi: 10.1190/1.1442774.

René, R. M., 1986, Gravity inversion using open, reject, and "shape-at-anomaly" till criteria: Geophysics, 51, no. 4, 988-994, doi: 10.1190/1.1442157.

Reynolds, J.M., 1997, An Introduction to Applied and Environmental Geophysics: John Wiley and Sons.

Roy, K. K., 2008, Potential Theory in Applied Geophysics: Springer.

Roy, A., 1962, Ambiguity in geophysical interpretation: Geophysics, 27, no. 1, 90-99, doi: 10.1190/1.1438985.

Sharma, P.V., 1986, Geophysical Methods in Geology, 2nd edition: Elsevier Science, New York.

Sen, M. K., and P. L. Stoffa, 1995, Global optimization method in geophysical inversion: Elsevier.

Sen, M. K., and P. L. Stoffa, 2013, Global optimization method in geophysical inversion-2nd edition: Cambridge University Press.

Skeels, D.C., 1947, Ambiguity in gravity interpretation: Geophysics, 12, no. 1, 43-56, doi: 10.1190/1.1437295.

Simpson, R.W., R. C. Jachens, R.J. Blakely, and R.W. Saltus, 1986, A new isostatic residual gravity map of the conterminous United States with a discussion on the significance of isostatic residual anomalies: Journal of Geophysical Research, 91, 8348–8372.

Smith, R. S., J. B. Thurston, T. F. Dai, and I. N. MacLeod, 1998, iSPI—the improved source parameter imaging method: Geophysical Prospecting, 46, no. 2, 141–151, doi: 10.1046/j.1365-2478.1998.00084.x.

Srivastava, R. P., and M. K. Sen, 2009, Fractal-based stochastic inversion of poststack seismic data using very fast simulated annealing: Journal of Geophysics and Engineering, 6, 412-425, doi:10.1088/1742-2132/6/4/009.

Steenland, N. C., 1968, The geomagnetic gradiometer by H. A. Slack, V. M. Lynch, and L. Langan (Geophysics, October 1967, 877–892): Geophysics, 33, 680– 686, doi: 10.1190/1.1486915.

Talwani, M., J. L. Worzel, and M. Landisman, 1959, Rapid gravity computations for two-dimensional bodies with application to the Mendocino submarine fracture zone: Journal of Geophysical Research, 64(1), 49–59, doi: 10.1029/JZ064i001p00049.

Thompson, D. T., 1982, EULDPH: a new technique for making computer-assisted depth estimates from magnetic data: Geophysics, 47, 31–37, doi: 10.1190/1.1441278.

Thurston, J. B., and R. S. Smith, 1997, Automatic conversion of magnetic data to depth, dip, and susceptibility contrast using the SPI method: Geophysics, 62, 807– 813, doi: 10.1190/1.1444190.

Uieda, L., and V. C. F. Barbosa, 2012, Robust 3D gravity gradient inversion by planting anomalous densities: Geophysics, 77, no. 4, G55–G66, doi: 10.1190/geo2011-0388.1.

Zidarov, D., and Zh. Zhelev, 1970, On obtaining a family of bodies with identical exterior fields method of bubbling: Geophysical Prospecting, 18, no. 1, 14-33, 10.1111/j.1365-2478.1970.tb02092.x.

Zhdanov, M. S., 2002, Geophysical inverse theory and regularization problems: Elsevier Science Publishing Co.

Appendix A - Derivatives of gravity field in Talwani's formula

Gravity anomaly and gravity gradient can be calculated using formulas derived in section 3.3 for a complex body. We here described the formula to calculate the derivatives of higher order using Talwani's method. All the terms written in the formula are the same as used in section 3.3. Based on the formula for the gravity, we describe now the equation that can be used to calculate the horizontal derivative of the field ($\partial g/\partial x$).

$$\left(\frac{\partial g}{\partial x}\right)_i = \sum_{q=1}^{Q}\left[\left\{\frac{-\alpha_q}{1+\alpha_q^2}\left(\log\frac{r_{q+1}}{r_q} - \alpha_q(\theta_{q+1}-\theta_q)\right)\right\} + \frac{\beta_q}{1+\alpha_q^2}\left\{\left(\frac{(x_q-\overline{x_\iota})}{r_q^2} - \frac{(x_{q+1}-\overline{x_\iota})}{r_{q+1}^2}\right) - \alpha_q\left(\frac{(z_{q+1}-\overline{z_\iota})}{r_{q+1}^2} - \frac{(z_q-\overline{z_\iota})}{r_q^2}\right)\right\}\right]. \quad (A.1)$$

Taking the derivative of $\partial g/\partial z$ vs. z, we give here the expression for the second-order vertical derivative ($\partial^2 g/\partial z^2$):

$$\left(\frac{\partial^2 g}{\partial z^2}\right)_i = \sum_{q=1}^{Q}\left[\frac{2\alpha_q}{1+\alpha_q^2}\left\{\left(\frac{(z_q-\overline{z_\iota})}{r_q^2} - \frac{(z_{q+1}-\overline{z_\iota})}{r_{q+1}^2}\right) - \alpha_q\left(\frac{(x_q-\overline{x_\iota})}{r_q^2} - \frac{(x_{q+1}-\overline{x_\iota})}{r_{q+1}^2}\right)\right\} + \frac{\beta_q}{1+\alpha_q^2}\left\{\left(\frac{1}{r_{q+1}^2} - \frac{1}{r_q^2} + \frac{2(z_q-\overline{z_\iota})^2}{r_q^4} - \frac{2(z_{q+1}-\overline{z_\iota})^2}{r_{q+1}^4}\right) - \alpha_q\left(\frac{2(x_q-\overline{x_\iota})(z_q-\overline{z_\iota})}{r_q^4} - \frac{2(x_{q+1}-\overline{x_\iota})(z_{q+1}-\overline{z_\iota})}{r_{q+1}^4}\right)\right\}\right]. \quad (A.2)$$

Taking the derivative of equation A.1 vs. z, we give here the expression for the second-order derivative $\partial^2 g/\partial z \partial x$:

$$\frac{\partial^2 g}{\partial z \partial x} = \sum_{q=1}^{Q} \left[\frac{-\alpha_q}{1+\alpha_q^2} \left\{ \left(\frac{(z_q - \overline{z_\iota})}{r_q^2} - \frac{(z_{q+1} - \overline{z_\iota})}{r_{q+1}^2} \right) - \alpha_q \left(\frac{(x_q - \overline{x_\iota})}{r_q^2} - \frac{(x_{q+1} - \overline{x_\iota})}{r_{q+1}^2} \right) \right\} \right.$$
$$+ \frac{\alpha_q}{1+\alpha_q^2} \left\{ \left(\frac{(x_q - \overline{x_\iota})}{r_q^2} - \frac{(x_{q+1} - \overline{x_\iota})}{r_{q+1}^2} \right) - \alpha_q \left(\frac{(z_{q+1} - \overline{z_\iota})}{r_{q+1}^2} - \frac{(z_q - \overline{z_\iota})}{r_q^2} \right) \right\}$$
$$+ \frac{\beta_q}{1+\alpha_q^2} \left\{ \left(\frac{2(x_q - \overline{x_\iota})(z_q - \overline{z_\iota})}{r_q^4} - \frac{2(x_{q+1} - \overline{x_\iota})(z_{q+1} - \overline{z_\iota})}{r_{q+1}^4} \right) \right.$$
$$\left. \left. - \alpha_q \left(\frac{1}{r_q^2} - \frac{1}{r_{q+1}^2} - \frac{2(z_q - \overline{z_\iota})^2}{r_q^4} + \frac{2(z_{q+1} - \overline{z_\iota})^2}{r_{q+1}^4} \right) \right\} \right]. \qquad (A.3)$$

Differentiating $\partial^2 g/\partial z^2$ we conclude with the expression valid for the third-order vertical derivative of the field:

$$\left(\frac{\partial^3 g}{\partial z^3}\right)_i = \sum_{q=1}^{Q}\left[\frac{3\alpha_q}{1+\alpha_q^2}\left\{\left(\frac{1}{r_{q+1}^2} - \frac{1}{r_q^2} + \frac{2\left(z_q-\overline{z_\iota}\right)^2}{r_q^4}\right.\right.\right.$$
$$\left. - \frac{2\left(z_{q+1}-\overline{z_\iota}\right)^2}{r_{q+1}^4}\right) - \alpha_q\left(\frac{2\left(x_q-\overline{x_\iota}\right)\left(z_q-\overline{z_\iota}\right)}{r_q^4}\right.$$
$$\left.\left. - \frac{2\left(x_{q+1}-\overline{x_\iota}\right)\left(z_{q+1}-\overline{z_\iota}\right)}{r_{q+1}^4}\right)\right\}$$
$$+ \frac{\beta_q}{1+\alpha_q^2}\left\{\left(\frac{6\left(z_{q+1}-\overline{z_\iota}\right)}{r_{q+1}^4} - \frac{6\left(z_q-\overline{z_\iota}\right)}{r_q^4} + \frac{8\left(z_q-\overline{z_\iota}\right)^3}{r_q^6}\right.\right.$$
$$\left. - \frac{8\left(z_{q+1}-\overline{z_\iota}\right)^3}{r_{q+1}^6}\right)$$
$$- \left(\frac{2\left(x_{q+1}-\overline{x_\iota}\right)}{r_{q+1}^4} - \frac{2\left(x_q-\overline{x_\iota}\right)}{r_q^4} + \frac{8\left(x_q-\overline{x_\iota}\right)\left(z_q-\overline{z_\iota}\right)^2}{r_q^6}\right.$$
$$\left.\left.\left. - \frac{8\left(x_{q+1}-\overline{x_\iota}\right)\left(z_{q+1}-\overline{z_\iota}\right)^2}{r_{q+1}^6}\right)\right\}\right]. \qquad (A.4)$$

Equations A.1, A.2, A.3 and A.4 may be used as themselves or for calculations of the scaling function of high order.